Journal of Materials Science & Technology 236 (2025) 198–214

Contents lists available at ScienceDirect

Journal of Materials Science & Technology

journal homepage: www.elsevier.com/locate/jmst

Research Article

Effect of powder preparation on degradation behavior and cytotoxicity of sintered porous biodegradable FeMnC alloys for biomedical applications

Abdelhakim Cherqaoui[a], Francesco Copes[a], Carlo Paternoster[a], Simon Gélinas[b], Paolo Mengucci[c], Carl Blais[b], Diego Mantovani[a,*]

[a] Laboratory for Biomaterials and Bioengineering, CRC-I, Department of Min-Met-Materials Eng., & University Hospital Research Center, Regenerative Medicine, Université Laval, QC, Canada
[b] Laboratory for Powder Metallurgy, Department of Min-Met-Materials Engineering, Université Laval, QC, Canada
[c] Department SIMAU & UdR INSTM, Università Politecnica Delle Marche, Via Brecce Bianche 12, 60131, Ancona, Italy

ARTICLE INFO

Article history:
Received 20 December 2024
Revised 15 March 2025
Accepted 16 March 2025
Available online 2 April 2025

Keywords:
Biodegradable FeMnC alloys
Powder metallurgy
Mechanical-milling
Degradation
Cell viability
Hemolysis

ABSTRACT

Biodegradable implants have emerged in biomedical applications, particularly for orthopedic fixations, cardiovascular stents, and tissue engineering scaffolds. Unlike permanent implants, they are designed to degrade and be reabsorbed after implantation in the body, mitigating the need for additional surgeries and reducing associated complications. In particular, Fe-Mn-C alloys constitute a new class of promising metallic materials for medical applications due to their outstanding mechanical properties and their biological performances. This study focuses on improving the degradation rates and cytotoxicity of sintered Fe-Mn-C alloys produced using the powder metallurgy process. To evaluate the impact of different powder preparation methods on material properties, two types of powders were used: (1) MX, prepared by mixing Fe, Mn, and C powders for 1 h; and (2) MM, obtained by mechanically milling the same powders for 10 h. Four mixtures with varying proportions of MX and MM were prepared. Two groups of samples were produced: one entirely from MX (A0), and another containing MM at 25 wt.% (A25), 50 wt.% (A50), and 75 wt.% (A75). All samples exhibited a complex microstructure comprising ferrite, martensite, and residual austenite. Degradation behavior assessment in Hanks' solution over 14 days showed that adding MM increased the degradation rate, from around 0.04 mmpy for A0 to 0.12 mmpy for A25. Notably, all samples showed similar cell viability, in the range of 83 %–89 % for 1 % extract dilution, and were non-hemolytic, with a hemolysis percentage below 1 %.

1. Introduction

Biodegradable implants have attracted increasing interest in biomedical applications, such as orthopedic fixations, cardiovascular stents, and tissue engineering scaffolds [1–3]. Unlike permanent implants, which often necessitate subsequent surgical removal and pose long-term risks like chronic inflammation and infection, biodegradable implants are designed to gradually degrade and be reabsorbed in the human body within a specific time frame, eliminating the need for additional procedures and reducing complications [4]. Generally, these medical devices require high mechanical performance. Considering these requirements, biodegradable metals (BMs) are often preferred over polymers and ceramics due to their superior mechanical strength and structural support [5].

Among BMs, Fe and Fe-based alloys have shown promise due to their excellent mechanical properties, good biocompatibility, and cost-effectiveness compared to other options like Mg and Zn. Mg alloys are often limited by their rapid degradation in physiological environments, while Zn alloys, despite their favorable degradation rate (DR), suffer from lower mechanical strength [6,7]. Additionally, Fe is an essential trace element in the human body for proper biological functions, especially for O transfer as reported by several authors [8–10]. Fe-based materials offer the potential to serve as structural supports that gradually degrade, allowing for the regeneration of the surrounding tissue. However, the primary

* Corresponding author.
E-mail address: diego.mantovani@gmn.ulaval.ca (D. Mantovani).

https://doi.org/10.1016/j.jmst.2025.03.016

challenge associated with Fe-based biodegradable materials is their slow and often uncontrolled degradation in physiological environments [2,11,12]. This limited degradation can delay the absorption of the implant and thus limit its clinical application. For instance, Kraus et al. [13] investigated the degradation behavior of two Fe-based alloys (Fe-10Mn-1Pd and Fe-21Mn-0.7C-1Pd) in vivo. They found that even after 52 weeks of implantation in a rat model, large portions of the implanted alloys remained, demonstrating the slow DR of Fe-based alloys in a biological environment. Therefore, enhancing the DR of Fe-based alloys while maintaining their mechanical integrity and biocompatibility remains a critical area of research.

Several strategies have been explored to address this issue, including alloying and advanced processing techniques [14,15]. Mn has been added to Fe-based alloys to design Fe-Mn systems, which exhibit enhanced DR due to Mn's electrochemical properties [16]. Moreover, Mn has been shown to reduce the ferromagnetic nature of pure Fe by stabilizing austenite, which is crucial for facilitating magnetic resonance imaging (MRI) during post-surgical follow-up [17,18]. For instance, the Fe-17Mn alloy developed by Jurgeleit et al. [19] showed improved corrosion and magnetic behavior compared to Fe-5Mn. In addition to Mn, C has been incorporated into Fe-based biodegradable alloys due to its grain refinement effect, which can influence corrosion behavior by modifying the microstructure [20].

Powder metallurgy (PM) techniques are attractive to produce BMs as they provide a means to fine-tune the microstructure, pore characteristics, and alloying element distribution, all of which are essential for optimizing the DR. Additionally, PM offers a cost-effective approach for manufacturing medical devices by enabling the direct production of net-shape or near-net-shape components with relatively complex geometries [21–23]. The porosity of these components can be precisely controlled in terms of amount, size, and distribution by optimizing the initial powder characteristics and processing parameters [24]. This, in turn, allows tailoring the mechanical properties and DR of BMs for biodegradable implant applications. For instance, Fe-Mn alloys produced by PM showed a faster in vitro DR compared to their cast counterparts, which is attributed to the inherent porosity of PM materials [25].

Among the various PM techniques, the conventional pressing and sintering process has been widely employed by several researchers [26–28] for preparing BMs. This process offers an optimal balance between simplicity, cost-effectiveness, and the ability to control the material's microstructure and porosity. In particular, the method used to prepare the starting powders significantly influences the final material properties. Prealloyed powders are preferred over elemental mixtures as they ensure a homogeneous element distribution, reduce segregation effects during sintering, and improve the reproducibility of material properties [29,30]. Moreover, prealloyed powders are particularly advantageous for sintering alloys containing volatile elements such as Mn, as prealloying reduces evaporation at high temperatures [31].

Various techniques exist for producing pre-alloyed metallic powders, including water atomization, gas atomization, and mechanical milling. Among them, mechanical milling offers distinct advantages for biodegradable metals, as it enables the production of ultrafine powders, which result in refined microstructures in sintered alloys. This microstructural refinement has been linked to enhanced degradation rates, as finer-grain structures degrade more uniformly and at a faster rate than coarse-grained counterparts [32].

This study aims to address the challenge of slow degradation in Fe-based biodegradable alloys by investigating the degradation behavior and in vitro cytotoxicity of sintered Fe-Mn-C alloys produced via conventional PM process (i.e., axial pressing and sintering). This later was chosen for manufacturing due to its ability to enhance the material's degradability through the incorporation of pores in the final sintered samples [21,33]. The novelty of this work lies in the combination of two powder preparation methods, namely mixing and mechanical milling, to produce Fe-Mn-C alloys with enhanced DR and acceptable cytotoxicity for biomedical implant applications. In this regard, two types of powders were considered: one was prepared by mixing pure elements (Fe, Mn, and C) for 1 h (MX), and the other was obtained by mechanically milling these elements for 10 h to produce a prealloyed Fe-Mn-C powder (MM). This composition was selected to achieve a fully austenitic structure, crucial for MRI compatibility [34], and to take advantage of the TWIP/TRIP effects conferred by high Mn contents, which improve mechanical performance [35,36]. Additionally, the selected Mn content is relatively low compared to that in many studies [37–39] of Fe-Mn-C biodegradable alloys, which typically contain around 30 wt.% Mn. This reduces the potential risk of neurotoxicity associated with excessive Mn exposure while maintaining adequate mechanical and degradation properties [40]. Therefore, MX and MM powders, which have distinct physical and electrochemical properties, were combined to evaluate the impact of the powder preparation method on the structural and microstructural characteristics of the sintered samples, as well as their degradation behavior and cytocompatibility. Four conditions were tested (A0: 0 wt.% MM, A25: 25 wt.% MM, A50: 50 wt.% MM, and A75: 75 wt.% MM) to systematically analyze the influence of MM powder addition on the alloy's performance.

2. Materials and methods

2.1. Samples preparation

For this study, two FeMnC powders with a nominal composition of 17 wt.% of Mn and 0.7 wt.% of C were prepared by mixing and mechanical milling processes. The starting materials included FeMn low-carbon ferromanganese powder (85 wt.% Mn, d_{50} = 62 µm), serving as a source of Mn, pure Fe powder (d_{50} = 45 µm, Rio Tinto), and synthetic graphite PG-25 (d_{50} = 10 µm, Rio Tinto). MX was produced by mixing the starting materials in a V-shell blender for 1 h. MM was prepared by dry milling the starting materials using a high-energy ball mill (UNI-BALL-MILL-II, Australian Scientific Instrument) at 120 RPM for 10 h. Milling was carried out in air using five stainless steel balls with a ball-to-powder ratio (BPR) of 6. To avoid the C solid solution hardening of the powder only 30 wt.% of the final C content was added during milling, while 70 wt.% was directly added to the milled powder, through a 30 min blending, before sintering.

Four different conditions were prepared by mixing MX and MM as presented in Fig. 1 and summarized in Table 1. The quantity of the MM was 0, 25, 50, and 75 wt.% to produce A0, A25, A50, and A75 samples, respectively. For each condition, 18 g of powder was compressed to form transverse rupture strength (TRS) bars as per MPIF standard [41] using a uniaxial hydraulic press (RK Machinery HFP 100, US) at 600 MPa. To aid compaction and facilitate sample

Table 1
Summary of the used powders and the sintered sample denominations.

Definition and nomenclature of the powders	
MX	Mixed powder
MM	Mechanically milled powder
Definition and nomenclature of the samples	
A0	Condition related to sintered samples with 100 wt.% MX
A25	Condition related to sintered samples with 25 wt.% MM + 75 wt.% MX
A50	Condition related to sintered samples with 50 wt.% MM + 50 wt.% MX
A75	Condition related to sintered samples with 75 wt.% MM + 25 wt.% MX

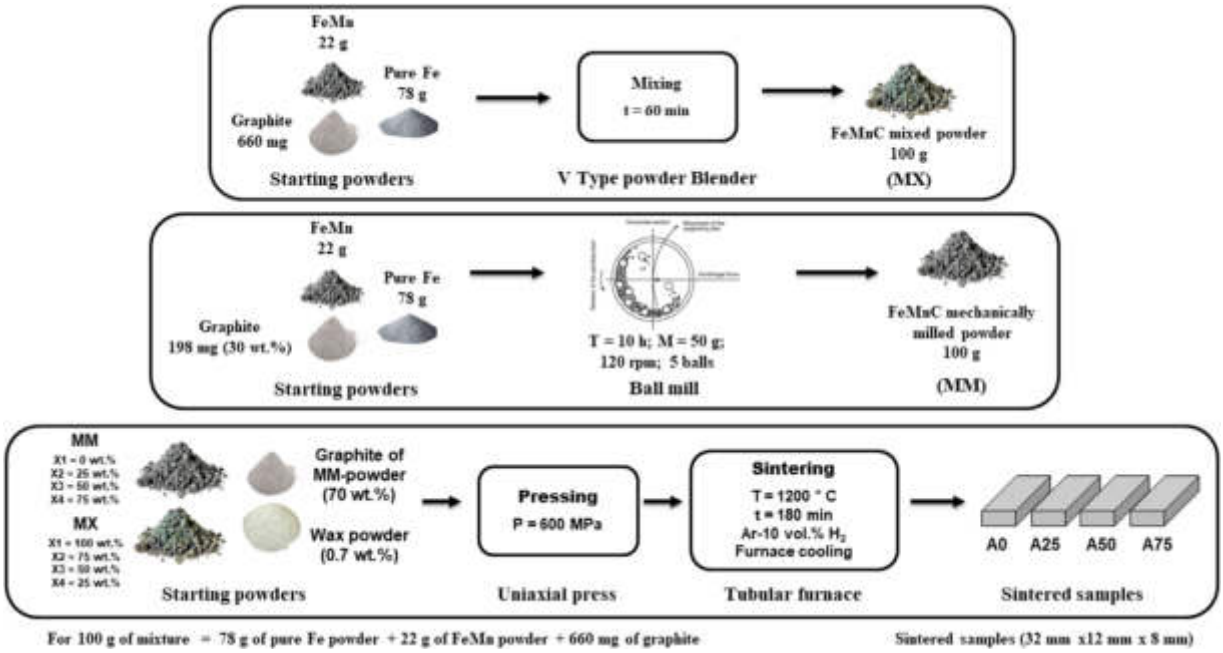

Fig. 1. Flowchart of the methodology and the production processes of MX, MM, and sintered samples including A0, A25, A50, and A75.

ejection from the die during the pressing stage, 0.7 wt.% of WAX lubricant (Rio Tinto) was blended with the powder mix. The final stage involved sintering the green compacts in a tubular furnace (Nanoe Zetasinter, US) at 1200 °C for 3 h under Ar-10 vol.% H_2 followed by furnace cooling.

2.2. Chemical composition

Microwave plasma atomic emission spectroscopy (MP-AES) was performed using an Agilent Technologies 4100$^+$ MP-AES, upgraded to a 4200-torch system, to quantify the Fe and Mn content (wt.%) in both the starting powders and the final sintered samples. The C and O amounts (wt.%) were determined using inert gas fusion for oxygen/nitrogen analysis (LECO ONH836) and combustion analysis for carbon/sulfur (LECO CS200), respectively.

2.3. Powder characterization

The morphology of both MX and MM was examined using a FEI Quanta 250 scanning electron microscope (SEM) equipped with an EDAX-Ametec energy-dispersive spectroscopy (EDS) system. EDS mapping was performed to assess the elemental distribution within the powder particles. The particle size distribution of the powders was measured using a laser particle size analyzer (Mastersizer 2000, Malvern Instruments). To determine the flow rate and apparent density of the starting powders, a Hall Flowmeter Funnel (QPI-HFM1800SS model) was employed, following ASTM standard B213–20 [42]. The apparent density of the powders (ρ_{app}) was calculated following ASTM standard B212–21 standard [43]. The results were reported to the nearest 0.01 g cm^{-3} and presented as the mean value of ρ_{app} considering five measurements.

2.4. Structural and microstructural characterization

An Olympus PME3 optical microscope (OM) was used to characterize the microstructure of the sintered alloys following chemical etching with a 2 % Nital solution. The crystallographic structure of these samples was characterized through X-ray diffraction (XRD) using a Brentano-Bragg geometry Bruker D8 Advance diffractometer with a Cu tube. The system included a graphite monochromator and operated at $V = 40$ kV and $I = 40$ mA, scanning over an angular range $2\theta = 20°–80°$. The XRD patterns were analyzed using the DIFFRAC.EVA software, with peak indexing performed through the search/match function using the PDF2 database from the International Center for Diffraction Data (ICDD). XRD peak shape analysis was carried out using Origin-2024b software. To obtain quantitative information from the XRD investigations, Rietveld analysis of XRD patterns was carried out by using the MAUD software [44]. Rietveld refinement was performed considering the crystallographic structure of α-Fe, ε-Fe, and γ-Fe phases available in the database Crystallography Open Database (COD). Calibration measurement of the Al_2O_3 powder standard was used to determine the instrumental broadening for the specific Bruker D8 Advance diffractometer. The combination of such distinct analyses carried out by the software tools mentioned above allowed indexing the XRD patterns and quantifying the relative amount of the Fe phases present in the samples.

The average grain size (AGS) of the sintered alloys was determined from OM micrographs, following the ASTM E112 standard [45] using ImageJ software. The experimental density (g cm^{-3}), theoretical density (g cm^{-3}), and relative density (%) of sintered samples were calculated according to Eqs. (1–3), respectively:

$$ED = \frac{M_{AS}}{V_{AS}} \quad (1)$$

where ED is the experimental density (g cm^{-3}), M_{AS} (g) is the sample weight after sintering weighted with a 5-digit precision digital balance (Analytical Plus, Ohaus, USA), and V_{AS} (cm^3) is the sample volume after sintering measured with an electronic digital caliper (Ditron, China) with a measurement accuracy of ± 0.02 mm.

$$TD = \sum_{i=1}^{4} x_i \cdot d_i \quad (2)$$

where TD is the theoretical density (g cm^{-3}) of the 100 % bulk samples, x_i is the molar fraction (mol.%), and d_i is the density (g cm^{-3}) of the element *i*. *i* refers to Fe, Mn, C, and O.

$$RD = \frac{ED}{TD} \times 100 \quad (3)$$

where RD is the relative density (%) of the sintered samples.

2.5. Degradation

2.5.1. Static immersion tests

Static immersion degradation (SID) tests were conducted on sintered alloys (10 mm × 10 mm × 2 mm) according to ASTM G31–21 standard [46]. The samples were polished to 800 grit and weighed. Three specimens per alloy were immersed in a modified Hanks' salt (MHS) solution, prepared using 9.4 g of balanced Hanks' salts, 14.16 g of HEPES acid, 16.65 g of HEPES sodium salt, and 3.3 g of sodium bicarbonate, dissolved in 1.4 L of deionized water. The pH of the solution was adjusted to 7.4 using 1 M of HCl or NaOH solutions. Each sample was suspended in 90 mL of solution at 37 ± 1 °C and 90 % relative humidity for 14 days. After SID tests, the samples were cleaned in ethanol and re-weighed to assess the DR. Samples DR was calculated based on the mass loss approach as per ASTM G31–21 [46] following Eq. (4):

$$DR = 8.76 \times 10^4 \times \frac{W}{A \cdot t \cdot \rho} \quad (4)$$

where DR is the degradation rate (mmpy), W is the mass loss (g), calculated as the difference between the sample weight before and after the SID test, A is the area of the sample (cm^2), t is immersion time (h) and ρ is the material density (ED, (g cm^{-3})). Values of DR were presented as mean value ± standard deviation (SD).

The testing solution, after 14 days of SID tests, was centrifuged to separate the degradation products (DPs) from the waste solution (supernatant). This later was analyzed using MP-AES to quantify released ions (Fe and Mn) content. Surface morphology of the degraded surfaces. As well as the DPs were examined using SEM (15 kV bias, W filament), while EDS analysis provided chemical composition data. Gold-platinum metallization was applied to improve the electrical conductivity of sample surfaces for SEM/EDS analysis. Additionally, DPs were identified using attenuated total reflectance Fourier transform infrared spectroscopy (FTIR). The analysis was performed using an Agilent Cary 660 FTIR spectrometer (Agilent Technologies, MN, USA), equipped with a deuterated L-alanine doped triglycine sulfate (DLa-TGS) detector and a germanium-coated KBr beam splitter. The FTIR measurements were recorded over a wavelength range of 4000–400 cm^{-1} with a resolution of 4 cm^{-1}. Fig. 2 shows the SID test setup and summarizes the post-characterization of degraded surfaces, DPs, and the supernatant.

2.5.2. Electrochemical measurements

Electrochemical measurements were carried out following ASTM G59–23 standard [47] on sintered samples measuring 10 mm × 10 mm × 2 mm in MHS solution at 37 ± 1 °C, maintained by a thermostatic bath. A three-electrode cell setup was used, consisting of a saturated calomel electrode as the reference, a graphite rod as the counter electrode, and the sample as the working electrode [48]. At least three samples of each alloy were tested. Before all electrochemical measurements, the open circuit potential (E_{OCP}) was stabilized for 1 h. Potentiodynamic polarization (PDP) tests were performed with a scan rate of 1 mV s^{-1}, over a potential range of −1 to 1 V relative to the E_{OCP}, with a step of 1 mV of voltage and 1 s of time. Electrochemical impedance spectroscopy (EIS) was conducted at the corrosion potential (E_{corr}) over a frequency range from 10^5 Hz to 10^{-2} Hz, with 10 data points per decade and an AC voltage amplitude of 10 mV peak-to-peak. The corrosion rate (CR) was determined following Eq. (5), based on the ASTM G59-23 standard [47]:

$$CR = 3.27 \times 10^{-3} \times \frac{i_{corr} \cdot EW}{\rho} \quad (5)$$

where CR is the corrosion rate (mmpy), i_{corr} is the current density (μA cm^{-2}) obtained using the Tafel extrapolation method on the potentiodynamic curves, EW is the equivalent weight (g) and ρ is the material density (ED, (g cm^{-3})).

2.6. In vitro biological characterization

2.6.1. Sample preparation

Indirect in vitro cytocompatibility and hemolysis tests were carried out to assess the cytocompatibility and hemocompatibility of the sintered samples, respectively. Pure Fe samples produced via the same process as described in Section 2.1 served as a control condition (CTRL). Before the test, all samples were mechanically polished up to 800 grit on both sides and sterilized by UV irradiation. Briefly, each side of the samples underwent 2 cycles (15 min each) of UV irradiation (254 nm). After that, samples were stored in a sterile 24 multi-well plate until use.

2.6.2. Indirect cytocompatibility assay

2.6.2.1. Cell culture. Human dermal fibroblasts (HDFs) were used in the following experiments. Briefly, HDFs were cultured in Dulbecco's modified Eagle's medium (D-MEM) with 10 % foetal bovine serum (FBS), penicillin (100 U mL^{-1}), and streptomycin (100 U mL^{-1}). Cells were maintained at 37 °C in a saturated atmosphere

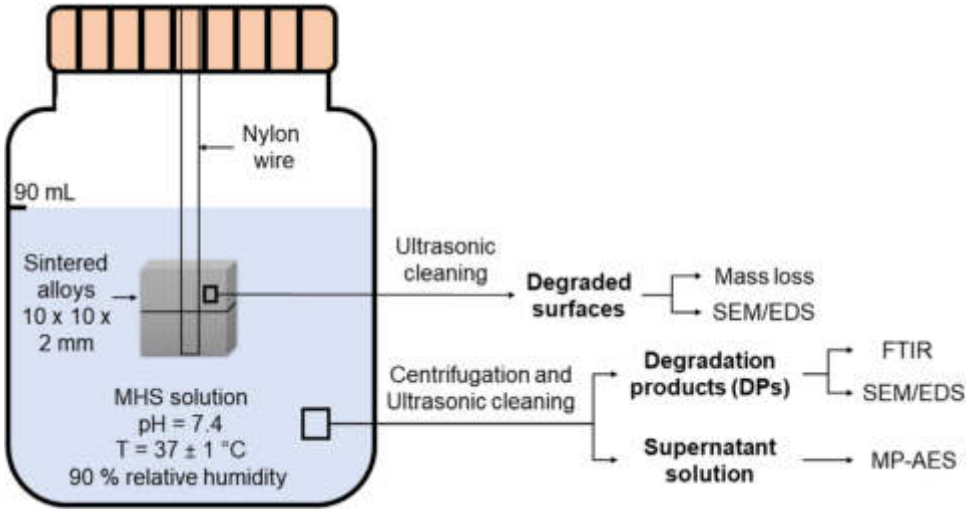

Fig. 2. Flowchart of 14 days SID test and post-characterization techniques of the degraded surfaces, DPs, and supernatant.

at 5 vol.% CO_2. Media was changed every two days until a 90 %–95 % confluence was reached. At this point, cells were detached from the plate using trypsin and then re-plated at a ratio of 1:5 or used for the experiments. Cells at passage 5 have been used for the present tests.

2.6.2.2. Indirect viability assay. The indirect cytotoxicity test was performed following the ISO 10993-5:2009 procedure [49]. 1 cm^2 samples were immersed in 660 µL of D-MEM culture medium, supplemented with 1 vol.% penicillin-streptomycin for 1 day. After the incubation, the medium was collected from the samples and subsequently used for the viability test. These tests have been performed using different concentrations of the extracted media: respectively 100 %, 10 %, and 1 % dilutions. Before putting them in contact with cells, extracted media have been supplemented with 10 vol.% FBS. For the 10 and 1 vol.% dilution, extracted media were diluted with a complete D-MEM medium. One day before contact with the extract, HDFs were seeded in the well of a 96 multi-well plate at a density of 20,000 cells cm^{-2} and incubated at 37 °C and 5 vol.% CO_2 for 24 h in 100 µL $well^{-1}$ of complete D-MEM. Cell cultivated in a complete D-MEM medium were used as a control (CTRL Plast). The day after, the medium was removed, and 100 µL of the 100 %, 10 %, and 1 % extract dilutions were added to the well-containing cells and incubated for 24 h. The extracts were then removed, and 100 μL of 1 % solution of resazurin sodium salt in complete D-MEM medium was added to the cells and incubated for 4 h at 37 °C and 5 vol.% CO_2. After the incubation, the solutions containing the now reduced resorufin product were collected and fluorescence intensity at a 545 nm_{ex}/590 nm_{em} wavelength was measured with a SpectraMax i3x Multi-Mode Plate Reader. Fluorescence intensity is proportional to cell viability.

2.6.2.3. Statistical analysis. Statistical significance has been calculated using the ANOVA non-parametric Kruskal-Wallis method with Dunn post-test through the software InStat ™. Values of $p < 0.05$ or less have been considered significant.

2.6.3. Hemolysis test

Whole human blood from a healthy donor was collected in citrate-containing blood collection tubes. Each sample was placed in a 15 mL tube, and 10 mL of sterile PBS 1X was added to each tube. PBS 1X served as the negative control, while deionized H_2O was used as the positive control. Samples and controls were incubated at 37 °C for 30 min.

Meanwhile, the collected blood was diluted in PBS 1X to a final ratio of 4:5 (four parts citrated blood and five parts PBS 1X). After incubation, 200 μL of the diluted blood was added to each tube and carefully mixed by inversion. The samples and controls were then incubated at 37 °C for 1 h, with gentle mixing by inversion after 30 min.

At the end of the incubation, all tubes underwent centrifugation at 800 g for 5 min. The supernatant was collected, and 100 μL aliquots were transferred to a 96-well plate. The absorbance (OD) at a wavelength of 540 nm was recorded. Hemolysis was calculated as follows:

$$\text{Relative Hemolysis} = \frac{\text{OD sample} - \text{OD CTRL POS}}{\text{OD CTRL Pos} - \text{OD CTRL Neg}} \times 100 \quad (6)$$

where OD sample is the sample absorbance, OD CTRL Neg is the negative control absorbance and OD CTRL Pos is the positive control absorbance.

3. Results

3.1. Chemical composition

Table 2 presents the nominal chemical composition of MX, and the experimental chemical composition of MM and the sintered alloys, including A0, A25, A50, and A75. MM exhibits the highest O content, around 0.85 wt.%, likely due to surface oxidation during the 10 h milling process. C content is reduced in the sintered alloys, falling below the target of 0.7 wt.% C, most likely as a result of Fe oxide reduction during sintering. The MM condition displayed a higher O content compared to the A0 one. Furthermore, a loss of Mn was evident for the sintered alloys compared to the starting powders. This was particularly noticeable for A0, where the Mn content decreased to about 14 wt.% due to Mn evaporation during the sintering process. Notably, as the weight percentage of MM increased in the alloys, the Mn loss decreased, suggesting that MM played a role in reducing Mn evaporation.

3.2. Powder characterization

Fig. 3 shows the morphology and elemental distribution of the MX and MM powders analyzed through SEM and EDS mapping as described in Section 2.3. Both powders exhibited irregular particle shapes. Specifically, the MM powder displayed a satellite effect (Fig. 3(b1)), characterized by the presence of Fe/Mn oxides on its surface following oxidation during milling. Other authors have also reported this phenomenon for Fe-Mn milled powders, such as Xu et al. [50], who observed the formation of similar satellites after 5 h of mechanical milling of Fe-28 wt.% Mn powders. Moreover, MM demonstrated a smaller particle size compared to MX. The EDS maps revealed a homogeneous distribution of Fe and Mn within the MM powder (Fig. 3(b2)), indicating the successful formation of a pre-alloyed FeMnC powder after 10 h of milling. Contrarily, large, isolated particles of Fe and Mn were noticed in the case of MX, as shown in Fig. 3(a2).

Table 3 summarizes the physical characteristics of both MX and MM powders. The particle size distribution analysis shows that 10 h of milling produced finer particles in MM, with a median size (d_{50}) of approximately 55 µm. In contrast, MX exhibited a larger d_{50} of about 75 µm. The ρ_{app} of the powders was relatively low, measuring an average of 2.82 g cm^{-3} for MX and 2.62 g cm^{-3} for MM. However, the flowability test revealed that MM was not free-flowing due to its smaller particle size, while MX had a

Table 2
Nominal composition of MX and experimental chemical composition of MM, and sintered samples (wt.%).

Sample	Fe	Mn	C	O
MX	Bal.	17	0.7	–
MM	Bal.	17.627 ± 0.086	0.212 ± 0.001	0.847 ± 0.039
A0	Bal.	13.699 ± 0.308	0.427 ± 0.003	0.061 ± 0.009
A25	Bal.	15.341 ± 0.448	0.451 ± 0.003	0.198 ± 0.008
A50	Bal.	16.059 ± 0.337	0.363 ± 0.001	0.099 ± 0.001
A75	Bal.	17.159 ± 0.172	0.357 ± 0.006	0.104 ± 0.009

Table 3
MX and MM physical characteristics.

Parameter		MX	MM
Particle size distribution	d_{10} (µm)	28.62	6.11
	d_{50} (µm)	74.32	54.55
	d_{90} (µm)	162.69	133.64
Apparent density (g cm^{-3})		2.82	2.62
Flowability (s/50 g)		40.73	No flow

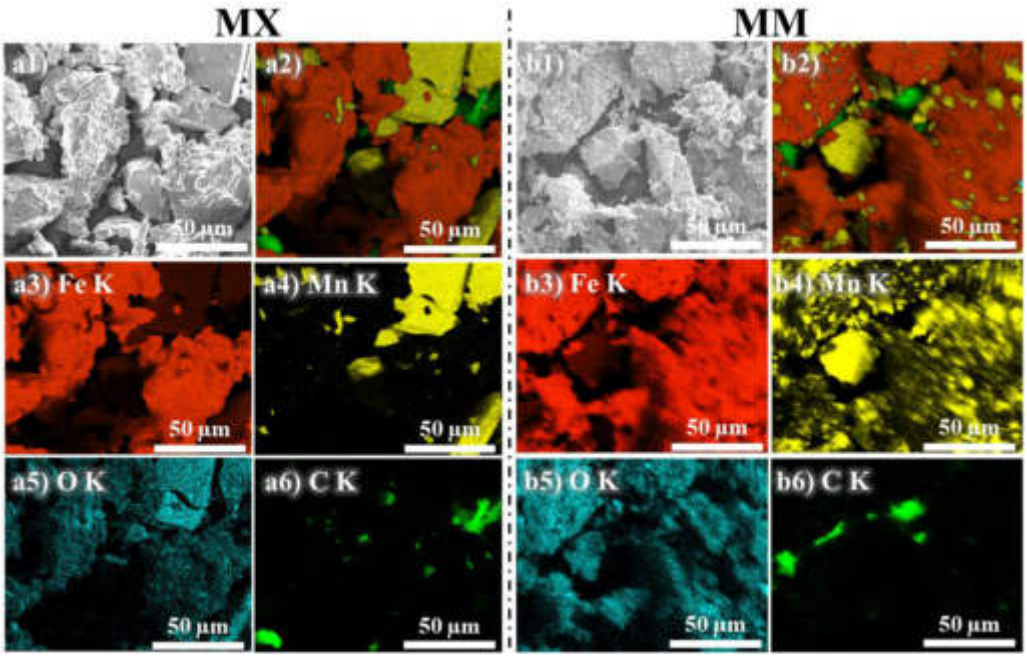

Fig. 3. SEM images and corresponding EDS maps: (a1) Secondary electron image of MX; (a2) color composite image showing the simultaneous distribution of (a3) Fe, (a4) Mn, (a5) O, and (a6) C for MX. (b1) Secondary electron image of MM; (b2) color composite image showing the simultaneous distribution of (b3) Fe, (b4) Mn, (b5) O, and (b6) C for MM.

reduced flowability, with a flow rate of 41 s/50 g. This may be mainly attributed to its irregular shape, which hindered a smooth flow.

3.3. Structural and microstructural characterization

Fig. 4 presents the microstructure of sintered samples, examined under OM at two magnifications, as described in Section 2.4. The A0 sample (Fig. 4(a)) revealed larger pores compared to those present in MM-containing samples. Its microstructure featured dispersed martensitic laths within ferrite regions, together with small equiaxed austenitic grains. In contrast, the A25 (Fig. 4(b)) and A50 (Fig. 4(c)) samples exhibited similar microstructures, comprising ferritic and martensitic zones with a minor presence of austenite. These samples showed significantly smaller pore sizes compared to the A0 sample. Finally, the A75 sample microstructure (Fig. 4(d))

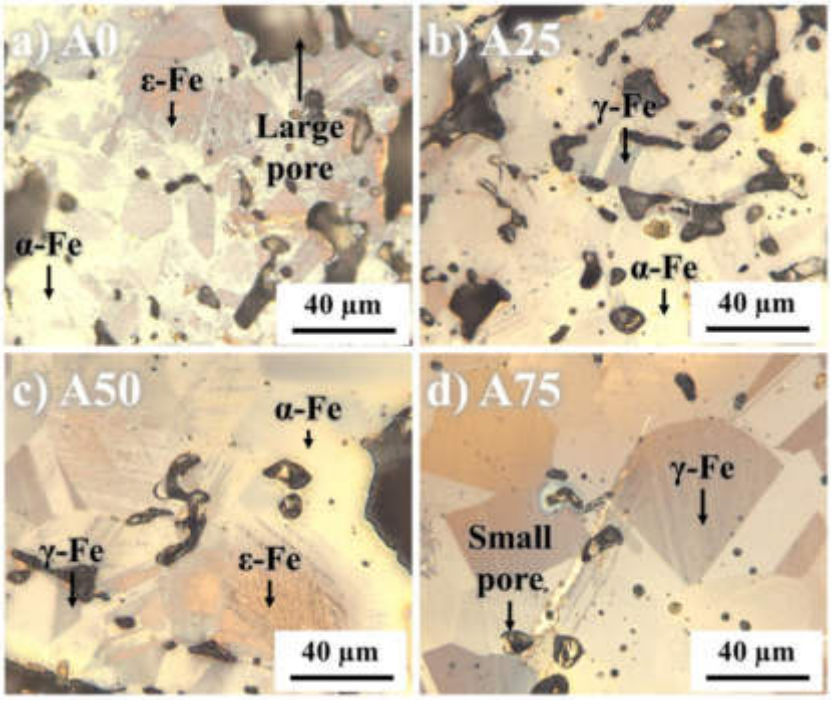

Fig. 4. OM micrographs of the cross sections of sintered samples after etching with Nital 2 %: (a) A0; (b) A25; (c) A50; (d) A75.

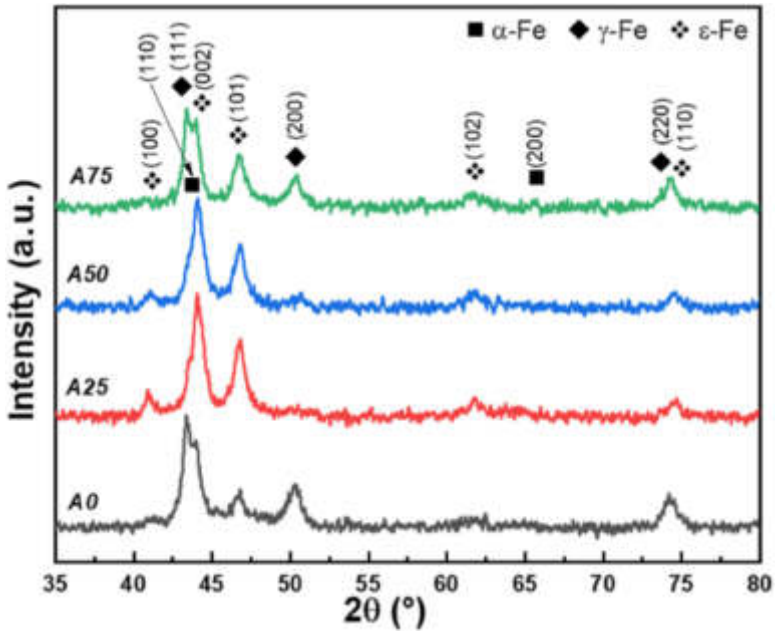

Fig. 5. XRD patterns of A0, A25, A50, and A75 sintered alloys.

demonstrated large equiaxed austenitic grains, adjacent to martensitic laths, with pores even smaller than those in the A25 and A50 samples.

XRD patterns of sintered samples are reported in Fig. 5, and to facilitate comparison, peaks were vertically adjusted. XRD analysis provided low-intensity patterns due to highly defective structures. In some patterns, the ferrite (α-Fe) peaks were very low; the α-Fe contributed to the high peak around 43°

Table 4 summarizes the structural and microstructural characteristics of sintered samples revealing distinct trends depending on their composition. A0 sample had a complex microstructure with almost equal proportions of ferrite, austenite, and martensite. A25 and A50 samples shared a similar phase composition, consisting mainly of ferrite and martensite with higher martensite (53 and 51 wt.%, respectively) and lower austenite (6 and 10 wt.%, respectively) contents. A75 condition showed a dual-phase microstructure, with 61 wt.% of austenite and 39 wt.% of martensite. Morphologically, the A0 sample had the largest AGS (30 µm) and average pore size (APS, 89 µm), but the lowest RD at approximately RD_{A0} = 76 %. For MM-containing samples, as the MM content increased, with a clear rise in both AGS and RD. However, the APS decreased as the MM amount increased. A25 and A50 conditions exhibited smaller grain sizes of around 12 µm for A25 and 19 µm for A50, with pore sizes of 27 and 21 µm, respectively. However, their RDs were slightly higher than that of the A0 condition, at RD_{A25} = 78 % and RD_{A50} = 80 %. The A75 sample, with an AGS of 22 µm and an APS of 19 µm, achieved the highest RD of RD_{A75} = 82 % among all samples.

3.4. Degradation

3.4.1. Static immersion

Fig. 6 shows the DRs measured after 14 days of SID tests in MHS solution, calculated using Eq. (4) as detailed in Section 2.5.1. The MM-containing samples exhibited notably higher DRs compared to the A0 samples, which demonstrated the lowest DR at approximately DR_{A0} = 0.036 ± 0.012 mmpy. Among the MM-containing group, the A25 sample had the highest DR, reaching DR_{A25} = 0.119 ± 0.011 mmpy, a value three times higher than that of the A0 samples, indicating a significant increase of DR with the addition of 25 wt.% MM. Interestingly, as the MM content increased, the DR progressively decreased, with the A75 sample showing the lowest DR among MM-containing samples at DR_{A75} = 0.061 ± 0.006 mmpy. The A50 sample exhibited a DR_{A50} = 0.082 ± 0.005 mmpy, falling between the A25 and A75 results.

The surface morphology of sintered samples before (Fig. 7(a–d)) and after (Fig. 7(e–l)) SID tests were analyzed using SEM in secondary electron mode. The DPs remaining on the sample surfaces are indicated by the white arrows in Fig. 7. For the four groups, these DPs appeared as small cubes agglomerated to form disconnected film-like layers, as seen in Fig. 7(j), or cluster-like shapes, such as those observed on the A50 sample surface (Fig. 7(k)). In this respect, DPs with similar morphologies were observed by Mouzou et al. [51] on the surface of a cast Fe-21Mn-1C after SID in MHS for 14 days. In the A0 samples, degradation initiated at the pore edges, with DPs accumulating mainly inside larger pores, as illustrated in Fig. 7(i). For the MM-containing group, DPs were

Table 4
Rietveld and structural analysis describing the microstructural features of each condition.

Sample	Weight fraction of different phases (wt.%)			AGS (µm)	RD (%)	APS (µm)
	α-Fe	γ-Fe	ε-Fe			
A0	25	47	30	29.69 ± 9.03	76.31 ± 0.20	89
A25	41	5.8	53	11.13 ± 3.22	77.36 ± 0.56	27
A50	40	9.8	51	18.26 ± 1.62	79.66 ± 1.17	21
A75	–	61	39	21.11 ± 3.36	81.18 ± 0.52	19

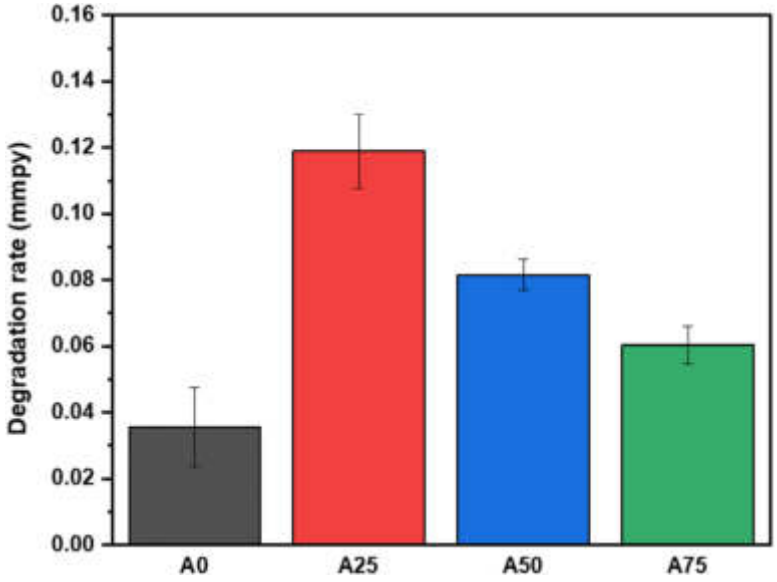

Fig. 6. Degradation rate of sintered samples after 14 days of SID tests in MHS solution.

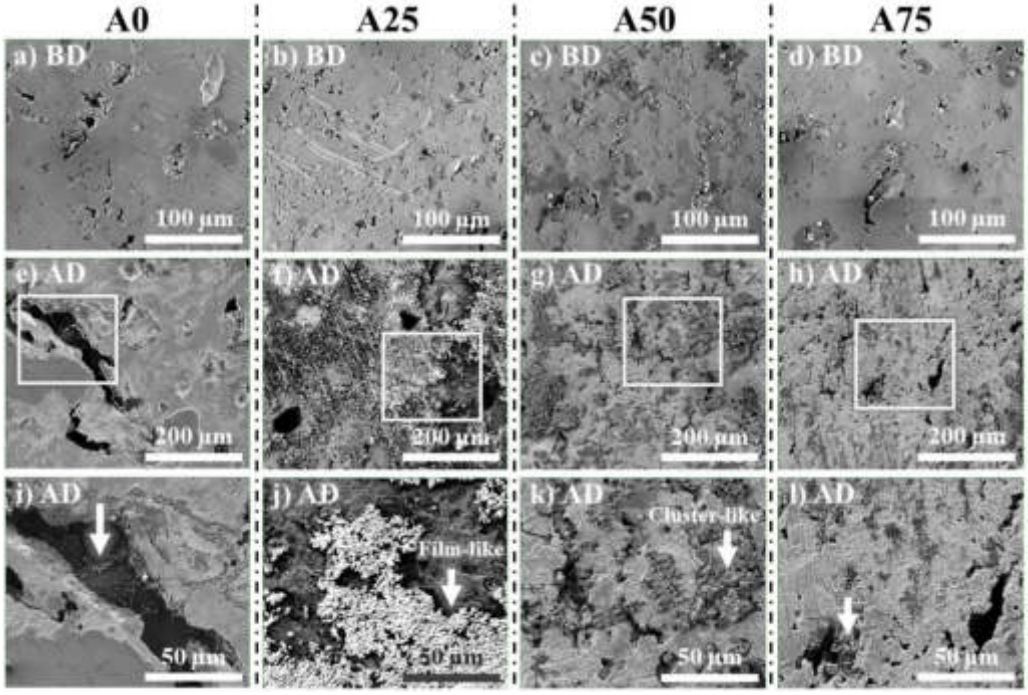

Fig. 7. Surface morphology of the cross-section of sintered samples before (BD) and after (AD) SID tests: A0 (a, e, i); A25 (b, f, j); A50 (c, g, k); A75 (d, h, l).

distributed irregularly on the surface of all the conditions (Fig. 7(j–l)), with some accumulation within larger pores. Notably, as the MM content increased from A25 to A75 samples, the surface coverage of DPs diminished, suggesting either a delay in degradation, thus reduced DPs formation, or that the formed DPs were more easily detached during ultrasonic cleaning prior to examination as described in Section 2.5.1.

Fig. 8 presents the elemental distribution across the degraded surfaces after SID tests, using EDS mapping. The maps corresponded to the micrographs at a 200 µm scale shown in Fig. 7(e–h), revealing mainly the presence of Fe, Mn, C, and O. The EDS maps for the four groups consistently showed the presence of these elements. Fe and Mn were homogeneously distributed on the surfaces without DP accumulation. In contrast, on the areas covered by DPs, the concentration of Fe was significantly lower or even absent compared to Mn, such as at large pore edges of the degraded A0 surface (Fig. 8(a2)). In these regions, O was concentrated, suggesting that the DPs remaining on the sample surfaces after SID tests were mainly in the form of Fe/Mn oxides and/or hydroxides. This observation is consistent with findings from other studies, such as in a recent work conducted by Limon et al. [52], which reported that DPs on degraded surfaces of a Fe-12Mn-1.2C alloy under similar conditions were mainly composed of Fe oxides (Fe_3O_4), Fe oxyhydroxide (FeO(OH)), and Mn oxides (Mn_2O_3, MnO_2, and Mn_3O_4).

To determine the chemical composition and the nature of the DPs detached into the solution after 14 days of SID tests (Fig. 9(a–d)), EDS and FTIR analyses were conducted, as shown in Fig. 9(e,

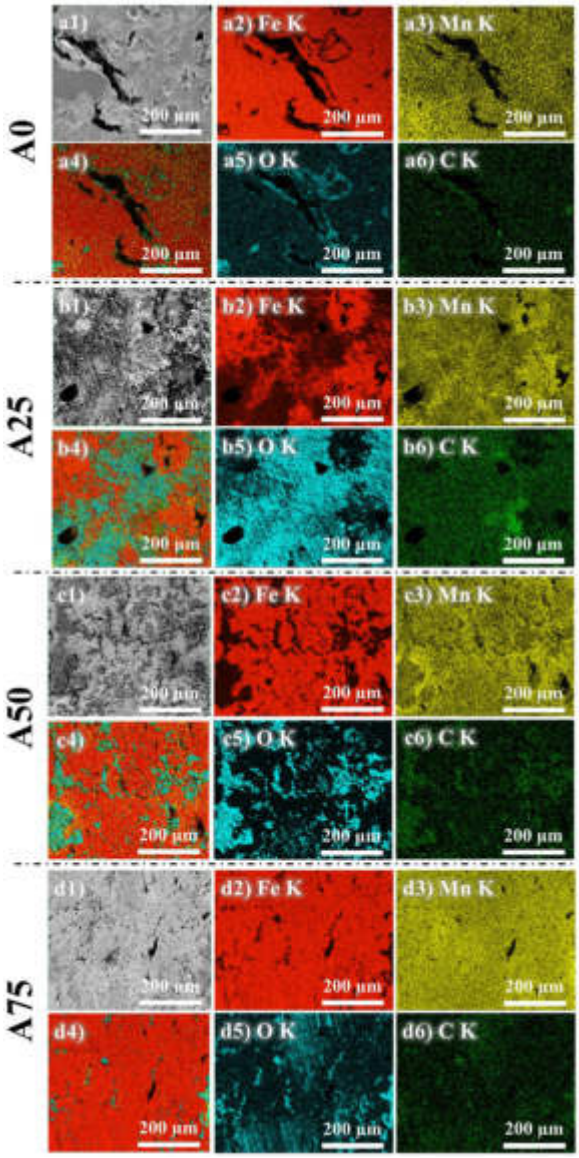

Fig. 8. SEM images and corresponding EDS maps of the degraded surfaces: (a1) Secondary electron image of A0; (a4) color composite image showing the simultaneous distribution of (a2) Fe, (a3) Mn, (a5) O, and (a6) C for A0. (b1) Secondary electron image of A25; (b4) color composite image showing the simultaneous distribution of (b2) Fe, (b3) Mn, (b5) O, and (b6) C for A25. (c1) Secondary electron image of A50; (c4) color composite image showing the simultaneous distribution of (c2) Fe, (c3) Mn, (c5) O, and (c6) C for A50. (d1) Secondary electron image of A75; (d4) color composite image showing the simultaneous distribution of (d2) Fe, (d3) Mn, (d5) O, and (d6) C for A75.

f). The EDS spectra (Fig. 9(e)) revealed that all four sample groups exhibited similar chemical compositions, with O, Fe, Mn, and P as the predominant elements, suggesting that the DPs primarily consisted of Fe/Mn phosphates. This finding was further supported by the FTIR analysis (Fig. 9(f)), where a broad peak around 1060 cm^{-1}, corresponding to PO_4^{3-} was observed, consistent with previous studies [51,53]. Additionally, a sharp peak around 600 cm^{-1} in the FTIR spectrum indicated the presence of carbonate functional groups (CO_3^{2-}), suggesting the formation of also Mn and Fe carbonates during degradation [48]. Small amounts (below 5 at. %) of Na and Cl were also consistently detected in all DPs, as indicated in Fig. 9(e), indicating the possible formation of Cl-containing phases. The FTIR spectra (Fig. 9(f)) further revealed a peak around 1650 cm^{-1}, likely corresponding to OH^- stretching, and a weak band around 1900 cm^{-1}, which could be attributed to C–H bonds due to organic ligands, such as D-glucose present in the MHS solution used for the study [54]. A weak peak from background CO_2 was detected around 2350 cm^{-1}, while the broad peak at 3400 cm^{-1} was attributed to absorbed H_2O [48].

Fig. 10 presents the amounts of Fe and Mn ions released after 14 days of SID tests, as determined by MP-AES analysis (described in Section 2.5.1). Only the supernatant, free of DPs, was analyzed. Generally, the concentration of Fe ions in the solution was higher than that of Mn ions. Among the four conditions, A25 showed the highest release of both Fe and Mn, with approximately 30 ± 1.5 ppm and 23 ± 1.7 ppm, respectively. In contrast, the A0 sample had the lowest ion release, with Fe at 24 ± 0.1 ppm and Mn at 16 ± 0.6 ppm. For the MM-containing samples, the A75 sample released the least amount of Fe (25 ± 1.1 ppm) and Mn (18 ± 0.5 ppm), while the A50 sample released intermediate contents, with around 28 ± 1.1 ppm of Fe and 21 ± 1.5 ppm of Mn. This trend of released ions was consistent with the tendency of sample DRs presented in Fig. 6.

3.4.2. Electrochemical measurements

3.4.2.1. Potentiodynamic polarisation tests. To evaluate the electrochemical response of the sintered samples to polarization, PDP tests were conducted as detailed in Section 2.5.2. The evolution of E_{OCP} over time is shown in Fig. 11(a), where all samples initially exhibited a rapid change in potential before gradually stabilizing over 1 h. Fig. 11(b) presents the PDP curves, which displayed similar shapes, indicating that the four samples had semblable polarization behavior.

Table 5 summarizes the kinetic parameters related to the PDP curves presented in Fig. 11(b). According to this table, E_{OCP} for all samples stabilized around E_{OCP} = −750 mV. A0 condition exhibited the most passive behavior, characterized by the lowest corrosion current density ($i_{corr\text{-}A0}$ = 90.57 ± 1.23 µA cm^{-2}). In contrast, A25 displayed the most active behavior, with the highest corrosion current density of $i_{corr\text{-}A25}$ = 148.35 ± 9.26 µA cm^{-2}. For samples containing MM, their E_{corr} values were relatively similar, around E_{corr} = −790 mV. However, regarding i_{corr}, the A75 condition had the lowest value of approximately $i_{corr\text{-}A75}$ = 116.24 ± 11.99 µA cm^{-2}, while A50 i_{corr} was intermediate, falling between those of A25 and A75, at $i_{corr\text{-}A50}$ = 131.04 ± 6.43 µA cm^{-2}. Consequently, A25 showed the highest CR (CR_{A25} = 1.79 ± 0.11 mmpy), followed by A50 (CR_{A50} = 1.58 ± 0.08 mmpy) sample and then A75 (CR_{A75} = 1.41 ± 0.14 mmpy). In contrast, A0 exhibited the lowest CR among all samples (CR_{A0} = 1.26 ± 0.02 mmpy), confirming that the addition of MM contributed to an increase in CR, which was consistent with the results of SID tests (Fig. 6).

Regarding the kinetics of the anodic and cathodic reactions, the β_a and β_c slopes were relatively similar for all samples, with values of approximately 135 mV for β_a and 200 mV for β_c. This suggests that the metal dissolution and reduction reactions occurred with comparable kinetics, except for the A75 sample, where β_c was higher, that is around 300 mV. This indicated that the reduction reaction was faster for the A75 condition compared to the ones for the other conditions.

3.4.2.2. Electrochemical impedance spectroscopy. The EIS results were analyzed through Nyquist (Fig. 12(a, c, e, g)) and Bode (Fig. 12(b, d, f, h)) plots. Nyquist plots indicated that the observed loop was not centered on the real axis at high frequencies, suggesting that the interface behaved as a constant phase element (CPE) rather than an ideal capacitor. This behavior corresponded to the formation of a double layer in parallel with a polarization resistance, indicating that the electrochemical reaction involved a single time constant at this frequency range. At lower frequencies, a linear segment with a 45° angle was observed, indicative of diffusion-

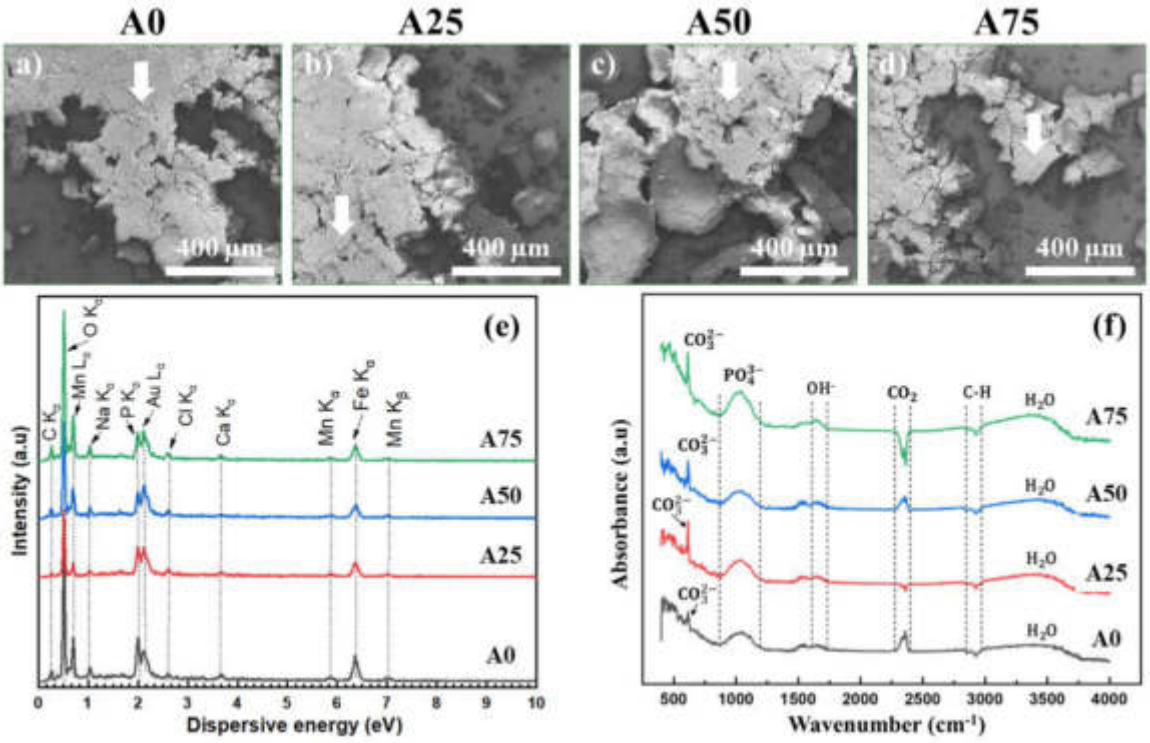

Fig. 9. SEM micrographs: (a) A0; (b) A25; (c) A50; (d) A75, and their corresponding EDS (e), and FTIR (f) patterns. The EDS patterns are related to the points indicated by arrows in (a–d).

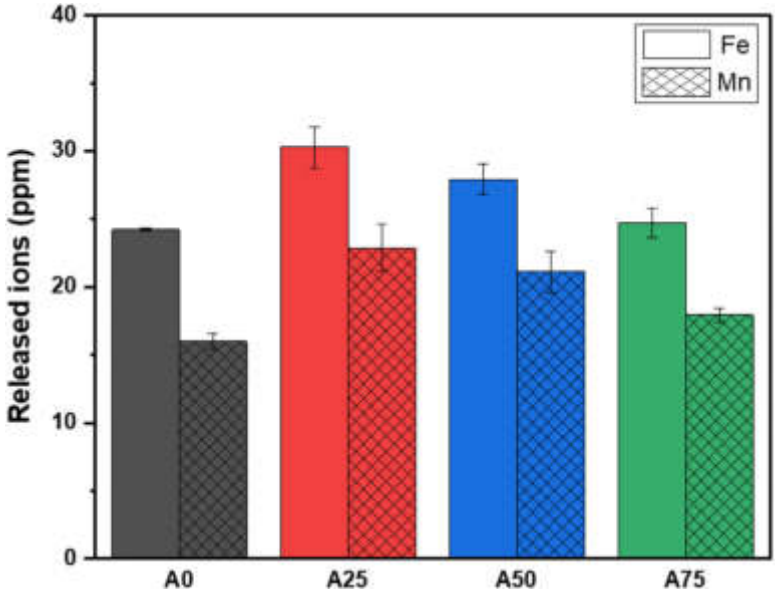

Fig. 10. Fe and Mn content in the supernatant after SID tests using MP-AES analysis.

Table 5
Summary of the corrosion data obtained from PDP tests for sintered samples in MHS solution.

Sample	E_{OCP} (mV)	E_{corr} (mV)	i_{corr} (µA cm^{-2})	β_a (mV)	β_c (mV)	CR (mmpy)
A0	−752.71 ± 11.46	−807.51 ± 13.50	90.57 ± 1.23	145.35 ± 1.77	200.91 ± 53.03	1.26 ± 0.02
A25	−752.15 ± 1.48	−793.57 ± 10.08	148.35 ± 9.26	139.46 ± 5.94	169.65 ± 5.59	1.79 ± 0.11
A50	−746.10 ± 10.18	−799.96 ± 5.45	131.04 ± 6.43	131.55 ± 1.06	190.25 ± 0.85	1.58 ± 0.08
A75	−754.12 ± 0.28	−788.41 ± 9.18	116.24 ± 11.99	128.73 ± 4.24	297.65 ± 84.07	1.41 ± 0.14

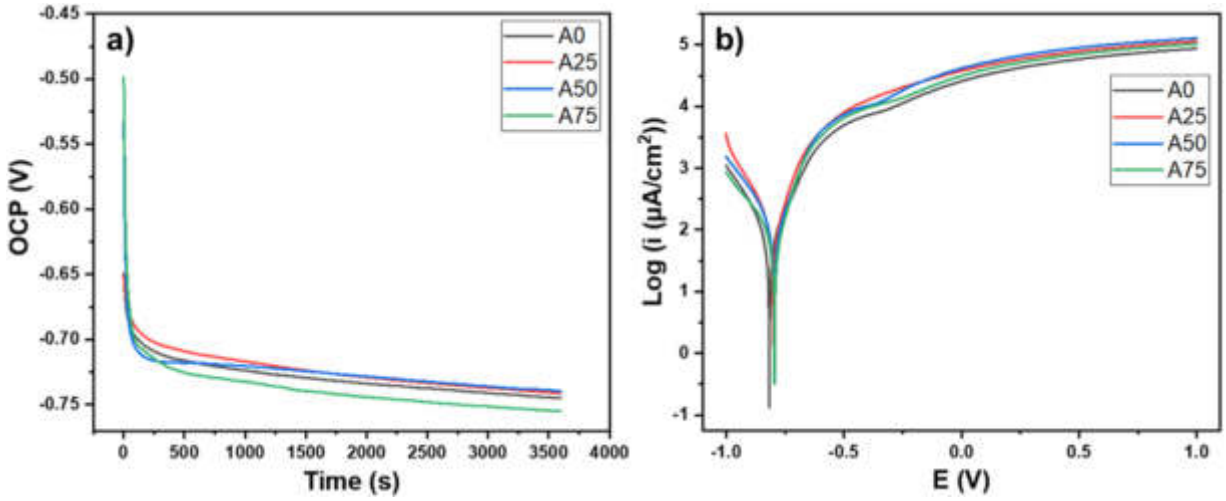

Fig. 11. Polarization curves of sintered samples in MHS solution: (a) the OCP curves; (b) The PDP curves.

Table 6
Electrochemical parameters obtained from the EIS technique for sintered samples in MHS solution.

Sample	R_s (Ω cm^2)	$Q_1 \times 10^{-6}$ (F s$^{(a1-1)}$)	a_1	R_1 (Ω cm^2)	W (Ω $s^{-0.5}$ cm^{-2})	$\chi^2/\|Z\|$
A0	18.81 ± 0.65	4.96 ± 0.91	0.51 ± 0.05	66.66 ± 3.34	14.79 ± 2.79	0.07 ± 0.02
A25	14.43 ± 0.23	4.69 ± 0.17	0.58 ± 0.06	35.57 ± 1.89	4.12 ± 0.58	0.04 ± 0.01
A50	13.20 ± 0.83	4.35 ± 0.12	0.58 ± 0.05	38.33 ± 0.86	4.01 ± 0.02	0.03 ± 0.01
A75	15.91 ± 0.16	2.23 ± 0.09	0.64 ± 0.04	54.85 ± 4.07	4.78 ± 0.48	0.04 ± 0.01

controlled processes. Bode plots further revealed two distinct time constants. The first, observed in the high-frequency range, corresponded to kinetically fast reactions associated with the formation of the double layer, while the second, occurring at low frequencies, was attributed to slower processes such as ion adsorption and diffusion. This dual-time-constant behavior suggested that an equivalent electrical circuit comprising a solution resistance (R_s), a CPE (Q_1, a_1), a charge transfer resistance (R_1), and a Warburg diffusion element (W) was the most appropriate for modeling the corrosion behavior of the samples. This circuit is schematized and joined to Nyquist plots in Fig. 12.

The electrochemical parameters extracted from the EIS data are summarized in Table 6. These data indicated a low variation of R_s across the samples, with A0 showing slightly higher R_s. This slight variation was possibly due to the dissolution of Fe and Mn during the 1 h stabilization of E_{OCP}. The diffusion coefficient parameter, a_1, approximates 0.5, characteristic of diffusion-controlled processes. R_1 was highest for A0, indicating a greater corrosion resistance, while A25 displayed the lowest R_1, suggesting more susceptibility to corrosion, followed by A50 and A75. This trend was consistent with the results of the SID (Fig. 6) and PDP (Table 5) tests. Here, it is worth mentioning that R_1 values could be influenced by interface heterogeneity, ion adsorption from the solution, and diffusion through surface pores. Additionally, the W provided insights into pore size distribution, with A0 exhibiting larger pores compared to A25, A50, and A75, which showed similar features with those evidenced by the structural characterization presented in Table 3.

3.5. Indirect cytocompatibility assay

Alamar blue viability tests have been performed on HDFs that have been put in contact with three different dilutions (100 %, 10 %, and 1 %) of extract obtained by the different samples to evaluate their effects on cell viability. This later was measured after 1 day of incubation using a resazurin salt solution assay. The results are presented in the graphic of Fig. 13 which shows the relative viability ± SD recorded from HDFs treated with the different experimental conditions. Results have been normalized against the CTRL Plast condition. For the 100 % dilution (pure extract), the A0, A50, and A75 conditions were able to significantly decrease the cell viability compared to the CTRL Plast ($p < 0.01$). Moreover, the viability recorded for A0 was also significantly reduced compared to the CTRL condition ($p < 0.01$). As for the 10 % dilution, the A0 ($p < 0.001$), A25 ($p < 0.01$), and A75 ($p < 0.05$) were able to significantly reduce the viability of the treated cells compared to the CTRL Plast condition. Once again, the A0 condition also showed significantly lower cell viability compared to the CTRL condition ($p < 0.05$). Finally, for the 1 % dilution, once again the A0 ($p < 0.01$), A25 ($p < 0.05$), and A75 ($p < 0.01$) showed a decreased cell viability compared to the CTRL Plast condition. No other significant differences were noted between the tested conditions. However, the cell viability of all samples improved with dilution, reaching over 80 % at a 1 % dilution. This level of viability qualifies the materials as cytocompatible, following the ISO 10,993/2009 standard [49].

3.6. Hemolysis test

Fig. 14 presents the hemolysis test results for the sintered samples, along with the control (CTRL), which consisted of pure Fe samples produced using the same process, as described in Section 2.6.1. The hemolysis percentage for all investigated samples was below 1 %, indicating that they did not induce hemolysis, which is common for Fe-based biomedical alloys. According to the ASTM F756–17 standard [55], a material is considered hemolytic if it induces a hemolysis percentage higher than 5 %. Therefore, the tested alloys can be classified as non-hemolytic. No significant differences were observed among the different samples. The obtained results align with previous studies on the hemocompatibility of Fe-Mn-based alloys for biomedical applications. For instance, Bagha et al. [56] reported hemolysis percentages of approximately 3 % and 4 % for Fe-30Mn and Fe-30Mn-1Ag alloys, respectively, prepared by mechanical alloying.

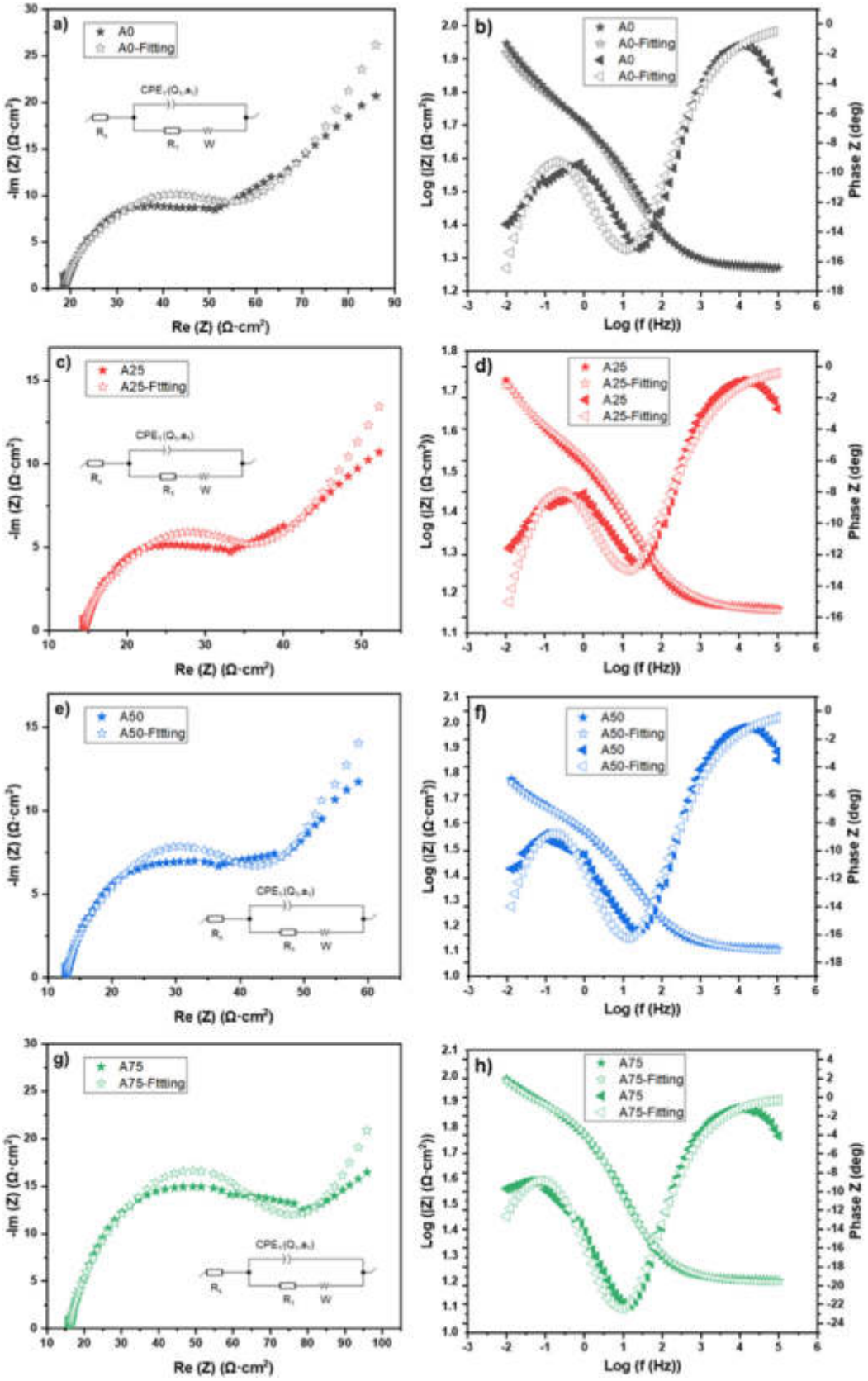

Fig. 12. (a–h) Nyquist and Bode diagrams of sintered samples in MHS solution.

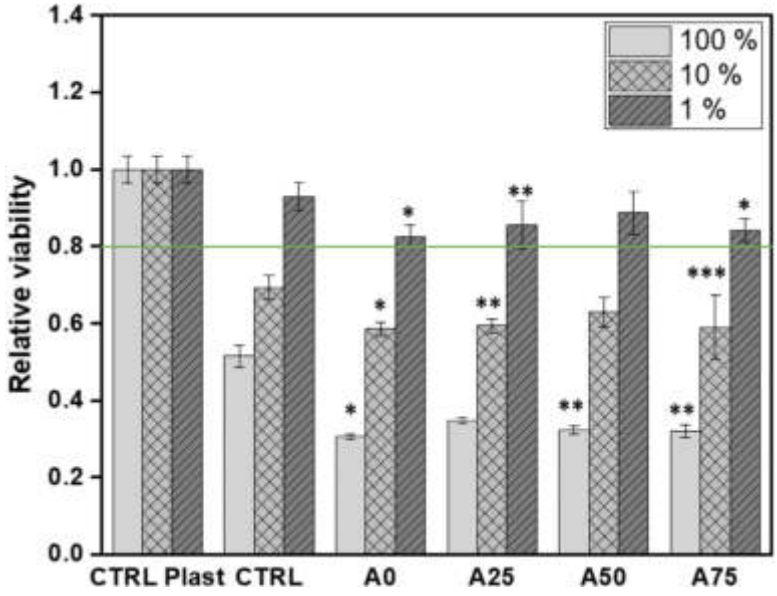

Fig. 13. Alamar Blue Viability Assay – 100 %, 10 %, and 1 % Dilutions. HDFs were treated with the following samples: standard culture medium (CTRL Plast); extract from control pure Fe samples (CTRL); extract from A0 samples (A0); extract from A25 samples (A25), extract from A50 samples (A50), and extract from A75 samples (A75). For 100 vol.% dilution, $^{*}p < 0.01$ vs. CTRL Plast and CTRL; ** $p < 0.01$ vs. CTRL Plast. For 10 vol.% dilution, $^{*}p < 0.001$ vs. CTRL Plast and $p < 0.05$ vs. CTRL; ** $p < 0.01$ vs. CTRL Plast, *** $p < 0.05$ vs. CTRL. For 1 vol.% dilution, $^{*}p < 0.01$ vs. CTRL Plast; ** $p < 0.05$ vs. CTRL Plast.

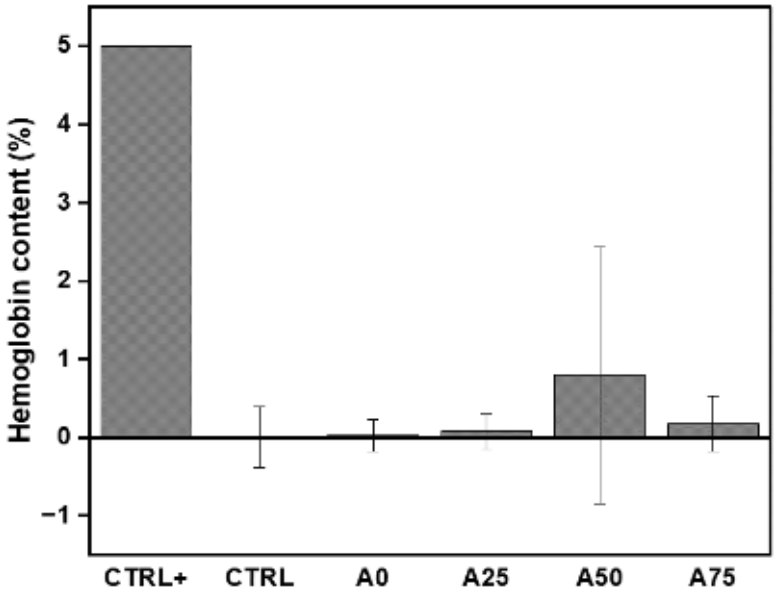

Fig. 14. Hemolysis test of the sintered samples (A0, A25, A50, and A75).

4. Discussion

4.1. Structural and microstructural characteristics

In this study, four groups of FeMnC samples were sintered from a mixture of MX and MM in different proportions, as described in Section 2.1. Both powders exhibited irregular particle shapes, as shown in Fig. 3, which is advantageous for the used production process (pressing and sintering) due to their tendency to interlock and increase green strength [57]. The MM powder showed a satellite effect, where smaller particles adhered to the surface of larger ones. In this regard, the chemical composition analysis revealed a higher O content in MM compared to MX. This phenomenon was attributed to the surface oxidation of MM during the 10 h of mechanical milling. This was also mentioned by other authors, such as Belaid et al. [58] who produced nanostructured FeMnC powders by mechanical alloying and noticed the formation of MnO after 24 h of milling even if it was performed in an Ar atmosphere.

The chemical analysis shown in Table 2 highlighted a noticeable trend in the Mn content, where the Mn amount in the starting powders was around 17 wt.%. However, in the sintered alloys, as the amount of MM decreased Mn content also decreased to approximately 13 wt.% in A0 samples as the proportion of MM was reduced from 75 wt.% in A75 samples to 0 wt.% in A0 samples. This reduction likely results from Mn evaporation during the sintering process, a phenomenon that has been reported in high-temperature sintering of Mn-containing alloys [59–61]. Similarly, the C content in the sintered samples was lower than the target (0.4 wt.% compared to the intended 0.7 wt.%), suggesting the potential loss of C due to the carbothermal reduction of Fe/Mn oxides

during sintering so-called *decarburization*. In this regard, it was reported that at higher temperatures (> 1000 °C) and in the presence of H_2, which was the case for the current work, the reduction of Mn oxides, especially MnO, may take place via Eqs. (7) and (8) [62].

$$MnO_{(s)} + H_{2(g)} \rightarrow Mn_{(s)} + H_2O_{(v)} \quad (7)$$

$$C_{(s)} + H_2O_{(v)} \rightarrow CO_{(g)} + H_{2(g)} \quad (8)$$

Moreover, Wang et al. [41] showed that at a high temperature of 1000 °C, Fe oxides such as Fe_2O_3 and Fe_3O_4 may undergo a carbothermal reduction via carbon monoxide [63].

Regarding the structure of the sintered samples, an increase in the RD was observed with a higher proportion of MM. However, this increase was not significant, possibly due to the particle size distribution of the MX and MM mixture. Finer MM particles could improve the compressibility of the mixture by filling the gaps between larger MX particles, as suggested by Hryha et al. [64]. The pore size also differed, with the A0 condition displaying the largest pore size (APS_{A0} = 30 µm). In contrast, MM-containing samples showed pore sizes around 20 µm, with a slight decrease as the amount of MM increased. This indicates that an increased MM content could lead to a more compact structure after sintering.

The phase composition of the sintered alloys varied depending on the amount of MM. For MM content up to 50 wt.% including A0, A25, and A50 samples, the microstructure was complex, comprising ferrite, austenite, and martensite phases. Notably, A0 exhibited a higher amount of residual austenite compared to A25 and A50 samples. This could be related to the stabilization mechanisms of the austenite phase influenced by the presence of free Mn. In this respect, Oh et al. [65] found that an increase in the Mn amount up to 10 wt.% in admixed Fe-Mn powder enabled the increase of residual austenite volume fraction in the final sintered samples. Conversely, the A75 sample displayed a dual-phase microstructure with 60 wt.% of austenite and 39 wt.% of martensite, indicating the effectiveness of 75 wt.% prealloyed MM in stabilizing the austenitic phase. These results and those of the chemical composition analysis (Table 2) were consistent with the Schuman diagram [66], except for A25 and A50, where no ferritic transformation was expected, however it took place. This might be due to the slow cooling mode (furnace cooling) that promotes the diffusion-controlled transformation of austenite into ferrite at lower temperatures as it was reported by Liang et al. [67]. Finally, the grain size analysis revealed that A0 samples had larger grains compared to MM-containing samples. In these later, the grain size increased with the amount of MM, which could be due to the formation of larger equiaxed austenitic grains during sintering.

4.2. Degradation

4.2.1. Degradation mechanism

All investigated samples exhibited the same degradation mechanism, which is one of Fe-Mn-based alloys in pseudo-physiological solutions, such as the MHS solution used in this study, which has been extensively studied by various researchers [52,53,68]. Generally, this mechanism involves electrochemical reactions at the material-electrolyte interface. This process consists of an anodic reaction, where the metal M (referring to Fe and Mn) dissolves into cations through oxidation (Eq. (9)), and a cathodic reaction (Eq. (10)), where dissolved oxygen consumes the electrons generated from Eq. (9) to form hydroxyl (OH^-) ions. Specifically, in Hanks' solution, Fe oxidizes into two forms: Fe^{2+} as described by Eq. (9), and Fe^{3+} as per Eq. (11) [48,69].

$$M_{(s)} \rightarrow M^{2+}{}_{(aq)} + 2e^- \quad (9)$$

$$O_{2(g)} + 2H_2O_{(l)} + 4e^- \rightarrow 4OH^-{}_{(aq)} \quad (10)$$

$$Fe^{2+}{}_{(aq)} \rightarrow Fe^{3+}{}_{(aq)} + 1e^- \quad (11)$$

Salama et al. [70] and several other authors [71,72] highlighted that in the presence of oxygen, metal ions (M^{2+}) from the anodic reaction react with hydroxyl ions produced in Eq. (10), leading to the formation of metal hydroxide $M(OH)_2$ following Eq. (12) and metal oxyhydroxide (MO(OH)), as in Eq. (13). $M(OH)_2$ subsequently transforms into a Fe/Mn oxide layer (mainly M_3O_4), Eq. (14), that limits further degradation. This agrees with the results found by EDS mapping carried out on degraded surfaces (Fig. 8), where Fe, Mn, and O were concentrated in the covered areas of these surfaces, suggesting that the deposited DPs were principally in the form of Fe/Mn oxides and oxyhydroxides. In a similar study, Huang et al. [73] found that Fe_2O_3 and $Fe(OH)_2$ were the main constituents of the DPs after 30 days of SID tests on pure iron samples.

$$M^{2+}{}_{(aq)} + 2OH^-{}_{(aq)} \rightarrow M(OH)_{2(s)} \quad (12)$$

$$2M^{2+}{}_{(aq)} + 4OH^-{}_{(aq)} \rightarrow H_{2(g)} + 2MO.OH_{(s)} \quad (13)$$

$$M(OH)_{2(s)} + 2MO(OH)_{(s)} \rightarrow M_3O_{4(s)} + 2H_2O_{(l)} \quad (14)$$

The MHS solution contains approximately 48 mg L^{-1} of phosphate ions ($HPO^{2-}{}_{4(aq)}$) and 1654 mg L^{-1} of carbonate ions ($HCO_3{}^-{}_{(aq)}$) [68]. Consequently, Fe/Mn phosphates and carbonates formed through Eqs. (15–20). This was confirmed by the chemical analysis (Fig. 9) of the degradation products (DPs) collected from the solution after the SID tests, which showed that these DPs primarily consisted of Fe/Mn phosphates with a smaller presence of carbonates. Similarly, Loffredo et al. [53] studied the degradation of a Fe16Mn0.7C cast alloy in MHS solution and found that after 14 days of SID under conditions comparable to this study, the main DPs were Fe/Mn phosphates and carbonates. Their FTIR analysis revealed that phosphate peaks were the most prominent, while carbonate and hydroxide peaks were generally weak.

$$HPO^{2-}{}_{4(aq)} \rightarrow PO^{3-}{}_{4(aq)} + H^+{}_{(aq)} \quad (15)$$

$$M^{2+}{}_{(aq)} + PO^{3-}{}_{4(aq)} \rightarrow M_3(PO_4)_2 \quad (16)$$

$$Fe^{3+}{}_{(aq)} + PO^{3-}{}_{4(aq)} \rightarrow FePO_{4(s)} \quad (17)$$

$$HCO^-{}_{3(aq)} \rightarrow CO^{2-}{}_{3(aq)} + H^+{}_{(aq)} \quad (18)$$

$$M^{2+}{}_{(aq)} + CO^{2-}{}_{3(aq)} \rightarrow MCO_{3(s)} \quad (19)$$

$$2Fe^{3+}{}_{(aq)} + 3CO^{2-}{}_{3(aq)} \rightarrow Fe_2(CO_3)_{3(s)} \quad (20)$$

The combined PDP (Fig. 11) and EIS (Fig. 12) results suggest that the corrosion mechanism of the investigated samples involved both uniform and localized electrochemical processes. Indeed, charge transfer and diffusion-controlled processes were indicated by dual-time constant behavior in EIS and similar PDP curve shapes. The stabilization of E_{OCP} around −750 mV suggested comparable thermodynamic corrosion tendencies, but the differences in current

densities (i_{corr}) indicated variations in reaction kinetics, as detailed in Section 3.4.2.1. The A0 condition exhibits a more stable passive behavior due to a higher polarization resistance (R_1), while the MM-containing samples (A25, A50, and A75) show increased surface reactivity, likely due to changes in microstructural and structural features.

4.2.2. Degradation rate

The incorporation of MM significantly increased the DR of the investigated Fe-Mn-C sintered alloys in the MHS solution. Both SID tests and electrochemical assessments (Section 3.4) revealed that MM-containing samples including A25, A50, and 75 M samples demonstrated higher DRs than the A0 samples, as shown in Fig. 6 and Table 5. This improvement can be attributed to the ability of the prealloyed MM to prevent Mn evaporation during the sintering process, resulting in a higher Mn content compared to the A0 condition, as detailed in Section 4.1. Notably, the electrochemical potential of Mn ($E_0 = -1.185$ V vs. SHE) is significantly lower than that of Fe ($E_0 = -0.447$ V vs. SHE). As a result, Mn effectively reduces the overall standard potential of Fe-Mn-based alloys by forming a solid solution with Fe, which in turn enhances the DR in pseudo-physiological solutions [7]. Therefore, samples containing MM, with their higher Mn content, 17 wt.% for A75, exhibited greater DRs compared to the A0 samples, which had a significantly lower Mn content at around 13 wt.%.

Variations in chemical composition, especially in Mn content, resulted in the formation of distinct microstructures with varying phase compositions and grain sizes, as outlined in Section 3.3. These variations likely explain the observed trend in CR for the MM-containing samples: A25 exhibited the highest CR (CR_{A25} =1.79 ± 0.11 mmpy), followed by A50 (CR_{A50} =1.58 ± 0.08 mmpy), and A75 with the lowest CR (CR_{A75} =1.41 ± 0.02 mmpy). It is well established that the CR of Fe-Mn-based alloys is directly proportional to the number of grain boundaries, which act as preferred sites for corrosion initiation [74]. For instance, in a previous study, Gebert et al. [75] found that in a *tris*-buffered simulated body fluid (SBF) solution, the degradation of a Fe-30Mn-1C alloy preferentially initiated at grain boundary regions. In the current study, the A25 samples showed the finest microstructure with an AGS of about 11 µm, resulting in the highest concentration of grain boundaries. In contrast, the A50 samples had a larger AGS of about 18 µm, while the A75 samples had the largest AGS of about 22 µm, leading to the lowest concentration of grain boundaries. Therefore, due to these differences in grain size, A25 is expected to be the most degradable alloy in the MHS solution, followed by A50 and then A75.

The variation in phase composition plays a crucial role in influencing the corrosion susceptibility of Fe-based alloys in pseudo-physiological solutions, as different phases with varying corrosion potentials are exposed to the degradation environment [48]. For example, austenite is known to be generally more corrosion-resistant than ferrite [76] and martensite [77]. Consequently, A75 sample, which contained a higher amount of austenite (61 wt.%), exhibited the lowest CR compared to A25 and A50. These latter samples had a more complex microstructure, predominantly composed of ferrite and martensite, with only a small amount (below 10 wt.%) of austenite. Additionally, the presence of multiple phases can lead to the formation of micro-galvanic corrosion cells, further promoting corrosion. For instance, Kumar et al. [78] demonstrated that in dual-phase steels containing ferrite and martensite, the CR was affected by the phase fractions and the creation of micro-galvanic cells. They found that ferrite acted as micro-anodic sites, while martensite served as micro-cathodic sites, leading to a general increase of the CR. As a result, the corrosion of A25 and A50 was more pronounced, as both ferrite and martensite acted as micro-anodic sites, while austenite acted as micro-cathodic sites, unlike in the A75 samples, where martensite was the only available micro-anodic site when micro-galvanic cells formed. The slightly higher CR observed for A25 compared to A50 could be attributed to its lower austenite content (around 6 wt.%), whereas A50 showed approximately twice that amount (about 10 wt.%).

The pore volume fraction and size are other factors influencing the DR of porous Fe-Mn-based alloys in MHS solution. For instance, Heiden et al. [79] reported that increased porosity and larger pore sizes in Fe30Mn, produced using the space holder technique to control porosity, led to higher long-term DRs than non-porous Fe30Mn. In the present study, the MM-containing samples exhibited comparable pore densities and sizes, approximately 20 vol.% and 22 µm, respectively. Therefore, the variations in DRs within this group are more likely attributed to microstructural characteristics. In contrast, the A0 sample had larger pores, with an APS of about 89 µm. However, its DR (DR_{A0} = 0.036 ± 0.012 mmpy) was three times lower than that of A25 (DR_{A25} = 0.119 ± 0.011 mmpy) when measured via SID tests. This discrepancy may be attributed to the accumulation of DPs within the larger pores of the A0 samples, as illustrated in Fig. 7(i). Consequently, the DR of the A0 sample might be underestimated when determined by the mass loss in SID tests. On the other hand, the results of PDP tests (Table 5) indicate that the CR of A25 was only 1.5 times that of A0. Since PDP tests do not involve the accumulation of DPs, this further supports the hypothesis that the DPs accumulation in SID tests led to an underestimation of the DR of the A0 sample, explaining why it appeared three times lower than that of A25.

4.3. In-vitro cytotoxicity

The cytotoxicity of the sintered alloys was assessed using an indirect cytotoxicity assay, as outlined in Section 2.6, and compared with pure Fe samples (CTRL). After 1 day of culturing HDFs with the extracts obtained by immersing the alloys in D-MEM, a significant decrease in cell viability was observed between the alloys and the CTRL Plast, as shown in Fig. 13 and described in Section 3.5. Despite this, no significant differences in cell viability were detected among the four sintered samples. The observed decrease in viability is likely due to the concentrations of Fe and Mn ions in the extracts. Previous studies on Fe-Mn alloys have similarly noted that decreased cell viability can be attributed to the release of Mn ions, whereas pure Fe and its released ions are non-toxic [72,80,81]. Released Mn ions were found to negatively impact cellular metabolism more than Fe ions [72]. For all sintered samples, after 14 days of static immersion testing, the concentration of released ions ranged from 24 to 30 ppm for Fe and 16 to 23 ppm for Mn (Fig. 10). This corresponded to a maximum release rate of 2.15 ppm day^{-1} (10.75 mg day^{-1}) for Fe and 1.64 ppm day^{-1} (8.2 mg day^{-1}) for Mn. These values were below the recommended daily intake limits of 45 mg day^{-1} for Fe and 11 mg day^{-1} for Mn [12]. Therefore, the amount of Fe and Mn ions released by immersion presented a low risk of adverse health effects, as the daily release of Mn (8.2 mg day^{-1}) approached but did not exceed its upper intake limit. The significant decrease in cell viability for A0 compared to the CTRL could be attributed to its higher porosity and larger pore size, leading to increased Mn ion release during incubation. Then, extracts from A0 consistently showed higher Mn ion concentrations compared to other conditions. In this context, Syarif et al. [82] reported that porous Fe-25Mn-1C samples exhibited lower cell viability compared to their denser counterparts produced through mechanical milling.

It is important to note that the used *in-vitro* model assesses cytotoxicity under static conditions, which do not consider dynamic factors present in a physiological environment, such as blood flow and continuous medium renewal. *In-vivo*, released ions and de-

tached DPs would disperse through blood flow, resulting in lower local ion concentrations around the biodegradable implant. Consequently, the extracts in this study contain higher ion concentrations than would occur under physiological conditions. To address this, two dilutions were applied (10 % and 1 %) by mixing extracts with D-MEM. Fig. 13 shows that cell viability increased with dilution, exceeding 70 % for all samples at 1 % dilution. This indicates that the cytotoxicity observed, for 100 % and 10 % dilutions, was not due to the inherent toxicity of the DPs or released ions, but rather to their concentration.

5. Conclusions

Prealloyed Fe-Mn-C powders (MM) were successfully produced through mechanical milling of elemental Fe, Mn, and C powders. The incorporation of MM powder led to an increase in the DRs of the sintered alloys. The relevant outcomes of this work could be summarized as follows:

(1) Increasing the MM content led to higher Mn levels in the final sintered alloys, while Mn evaporation during sintering was more significant in A0 samples, as MX was not prealloyed.
(2) A complex microstructure consisting of ferrite, austenite, and martensite was observed in the A0, A25, and A50 samples, while the A75 sample exhibited a dual-phase microstructure with approximately 60 wt.% austenite and 40 wt.% residual austenite.
(3) The MM-containing samples showed similar microstructural and structural characteristics, whereas the A0 samples had larger pore and grain sizes.
(4) The DR of the MM-containing samples was higher than that of the A0 samples, indicating MM's ability to enhance degradability. DPs that remained on the sample surfaces after the SID test were primarily in the form of Fe/Mn oxides and/or oxyhydroxides, while those released into the solution were mainly Fe/Mn phosphates and carbonates. EIS results indicated that the corrosion mechanism involved both localized and uniform corrosion.
(5) Cell viability was primarily influenced by the concentration of DPs and leached ions in the extracts rather than their composition. At 1 % dilution, all samples demonstrated high cell viability, exceeding 80 %, which is considered a favorable response for biodegradable Fe-based alloys.
(6) All the sintered samples were non-hemolytic exhibiting a hemolysis percentage lower than 1 %.

Declaration of competing interest

The authors declare that they have no known competing financial interests or personal relationships that could have appeared to influence the work reported in this paper.

CRediT authorship contribution statement

Abdelhakim Cherqaoui: Writing – review & editing, Writing – original draft, Visualization, Software, Methodology, Investigation, Formal analysis, Data curation, Conceptualization. **Francesco Copes:** Writing – original draft, Methodology, Investigation. **Carlo Paternoster:** Writing – review & editing, Writing – original draft, Validation, Conceptualization. **Simon Gélinas:** Writing – review & editing, Validation, Methodology, Investigation. **Paolo Mengucci:** Methodology, Investigation. **Carl Blais:** Writing – review & editing, Validation, Supervision, Conceptualization. **Diego Mantovani:** Writing – review & editing, Validation, Supervision, Resources, Conceptualization.

Acknowledgments

This work was mainly supported by the Natural Science and Engineering Research Council of Canada (Discovery and Alliance), and PRIMA (Quebec Ministry for Economy and Innovation). Diego Mantovani holds a Canada Research Chair Tier I (2012-2026).

References

[1] G. Chandra, A. Pandey, Biocybern. Biomed. Eng. 40 (2020) 596–610.
[2] G. Chandra, A. Pandey, Expert Rev. Med. Devices 18 (2021) 629–647.
[3] M. Prakasam, J. Locs, K. Salma-Ancane, D. Loca, A. Largeteau, L. Berzina-Cimdina, J. Funct. Biomater. 8 (2017) 44.
[4] R.D. Alexy, D.S. Levi, Biomed. Res. Int. 1 (2013) 137985.
[5] C. Shuai, S. Li, S. Peng, P. Feng, Y. Lai, C. Gao, Mater. Chem. Front. 3 (2019) 544–562.
[6] Y. Liu, Y. Zheng, X.H. Chen, J.A. Yang, H. Pan, D. Chen, L. Wang, J. Zhang, D. Zhu, S. Wu, Adv. Func. Mater. 29 (2019) 1805402.
[7] Y.F. Zheng, X.N. Gu, F. Witte, Mater. Sci. Eng. R. Rep. 77 (2014) 1–34.
[8] D. Vojtech, J. Kubasek, J. Capek, I. Pospisilova, Mater. Tehnol. 49 (2015) 877–882.
[9] B. Wegener, B. Sievers, S. Utzschneider, P. Müller, V. Jansson, S. Rößler, B. Nies, G. Stephani, B. Kieback, P. Quadbeck, Mater. Sci. Eng. B 176 (2011) 1789–1796.
[10] A. Yusop, A. Bakir, N. Shaharom, M. Abdul Kadir, H. Hermawan, Int. J. Biomater. 1 (2012) 641430.
[11] A. Alsakkaf, A.H.M. Yusop, H. Idris, A.G. Hassan, N. Iqbal, R. Unal, I. Sudin, Mater. Today Commun. 41 (2024) 110609.
[12] J. Venezuela, M. Dargusch, Curr. Opin. Solid State Mater. Sci. 24 (2020) 100822.
[13] T. Kraus, F. Moszner, S. Fischerauer, M. Fiedler, E. Martinelli, J. Eichler, F. Witte, E. Willbold, M. Schinhammer, M. Meischel, Acta Biomater. 10 (2014) 3346–3353.
[14] J. He, F.-L. He, D.-W. Li, Y.-L. Liu, Y.-Y. Liu, Y.-J. Ye, D.-C. Yin, RSC Adv. 6 (2016) 112819–112838.
[15] S. Loffredo, PhD. Thesis, Laval University, 2020.
[16] N. Cimpoeşu, F. Săndulache, B. Istrate, R. Cimpoeşu, G. Zegan, Metals 8 (2018) 541.
[17] Č. Donik, J. Kraner, A. Kocijan, I. Paulin, M. Godec, Sci. Rep. 11 (2021) 19506.
[18] D. Spandana, H. Desai, D. Chakravarty, R. Vijay, K. Hembram, Adv. Powder Technol. 31 (2020) 4577–4584.
[19] T. Jurgeleit, L.K. Jessen, E. Quandt, C. Zamponi, Materials 11 (2018) 482.
[20] B. Liu, Y. Zheng, Acta Biomater. 7 (2011) 1407–1420.
[21] P. Liu, D. Zhang, Y. Dai, J. Lin, Y. Li, C. Wen, Acta Biomater. 114 (2020) 485–496.
[22] V.M. Rabeeh, T. Hanas, Prog. Biomater. 11 (2022) 163–191.
[23] Z. Xu, M.A. Hodgson, P. Cao, Mater. Sci. Eng. A 630 (2015) 116–124.
[24] S. Parvizi, S.M. Hashemi, F. Asgarinia, M. Nematollahi, M. Elahinia, Prog. Mater. Sci. 117 (2021) 100739.
[25] M. Moravej, D. Mantovani, Int. J. Mol. Sci. 12 (2011) 4250–4270.
[26] A. Dehghan-Manshadi, D. StJohn, M. Dargusch, Materials 12 (2019) 1572.
[27] P. Goudarzi, M. Moazami-Goudarzi, A. Masoudi, Mater. Chem. Phys. 287 (2022) 126368.
[28] N. Tipan, A. Pandey, P. Mishra, Mater. Today Commun. 31 (2022) 103658.
[29] H.-x. Hu, W. Chen, C. Deng, J. Mater. Res. Technol. 12 (2021) 150–158.
[30] X. Zhao, J. Li, L. Duan, S. Tan, X. Fang, Int. J. Refract. Met. Hard Mater. 79 (2019) 115–122.
[31] M.C. Conti, B. Mallia, E. Sinagra, P.S. Wismayer, J. Buhagiar, D. Vella, Heliyon 5 (2019) 9.
[32] C.S. Obayi, P.S. Nnamchi, P.O. Offor, S.N. Ude, J. Nano Mater. Sci. Res. 2 (2023) 97–103.
[33] S. Mandal, S.K. Nandi, M. Roy, J. Mater. Chem. B 9 (2021) 4340–4354.
[34] M.H. Fritsch, Otol. Neurotol. 28 (2007) 733–738.
[35] M. Bordone, J. Perez-Ipiña, R. Bolmaro, A. Artigas, A. Monsalve, Metals 11 (2020) 24.
[36] B. Harsha, A. Patnaik, M. Banerjee, E. Kozeschnik, Mater. Today: Proc. 72 (2023) 1365–1371.
[37] S.M. Huang, E.A. Nauman, L.A. Stanciu, Mater. Sci. Eng. C 99 (2019) 1048–1057.
[38] M. Traverson, M. Heiden, L.A. Stanciu, E.A. Nauman, Y. Jones-Hall, G.J. Breur, Vet. Comp. Orthop. Traumatol. 31 (2018) 010–016.
[39] X. Wang, H. Zurob, J. Embury, X. Ren, I. Yakubtsov, Mater. Sci. Eng. A 527 (2010) 3785–3791.
[40] S.L. O'Neal, W. Zheng, Curr. Environ. Health Rep. 2 (2015) 315–328.
[41] Metal Powder Industries Federation, Standard test methods for Metal powders and Powder metallurgy products, Metal Powder Industries Federation, 2007.
[42] Standard Test Methods for Flow Rate of Metal Powders Using the Hall Flowmeter Funnel, ASTM B213-20, ASTM International, West Conshohocken, PA, 2020.
[43] Standard Test Method for Apparent Density of Free-Flowing Metal Powders Using the Hall Flowmeter Funnel, ASTM B212-21, ASTM International, West Conshohocken, PA, 2021.
[44] L. Lutterotti, Nucl. Instrum. Methods Phys. Res. Sect. B Beam Interact. Mater. Atoms 268 (2010) 334–340.
[45] Standard Test Methods for Determining the Average Grain Size of Metal Materials, ASTM E112, ASTM International, West Conshohocken, PA, 2004.
[46] Standard Guide for Laboratory Immersion Corrosion Testing of Metals, ASTM G31-12a, ASTM International, West Conshohocken, PA, 2012.

[47] Standard Test Method for Conducting Potentiodynamic Polarization Resistance Measurements, in: Annual Book of ASTM Standards, ASTM International, 2009, pp. 237–239.
[48] A. Cherqaoui, Q.N. Cao, M.L. Gatto, C. Paternoster, P. Mengucci, D. Mantovani, Bioact. Mater. 41 (2024) 96–107.
[49] Biological Evaluation of Medical Devices-Part 5, Tests For in Vitro Cytotoxicity, International Organization for Standardization (ISO), ISO 10993-5:2009, 2009.
[50] Z. Xu, M.A. Hodgson, P. Cao, J. Mater. Sci. Technol. 32 (2016) 1161–1170.
[51] E. Mouzou, C. Paternoster, R. Tolouei, P. Chevallier, C.A. Biffi, A. Tuissi, D. Mantovani, Mater. Lett. 181 (2016) 362–366.
[52] I. Limón, M. Multigner, C. Paternoster, M. Lieblich, B. Torres, D. Mantovani, J. Rams, Bioact. Mater. 40 (2024) 524–540.
[53] S. Loffredo, S. Gambaro, L. Marin de Andrade, C. Paternoster, R. Casati, N. Giguere, M. Vedani, D. Mantovani, ACS Biomater. Sci. Eng. 7 (2021) 3669–3682.
[54] J. Zhou, M. Fink, M. Bruns, Y. Yang, R. Detsch, A.R. Boccaccini, H. Ermert, S. Virtanen, Mater. Sci. Eng. C 95 (2019) 275–285.
[55] Standard Practice for Assessment of Hemolytic Properties of Materials, ASTM F756-17, ASTM International, West Conshohocken, PA, 2017.
[56] P.S. Bagha, M. Khakbiz, S. Sheibani, S. Ebrahimi-Barough, H. Hermawan, ACS Biomater. Sci. Eng. 6 (2020) 2094–2106.
[57] S. Allain, J.-P. Chateau, O. Bouaziz, S. Migot, N. Guelton, Mater. Sci. Eng. A 387 (2004) 158–162.
[58] L. Belaid, M. Bendoumia, M. Dakiche, H. Mechri, D. Dahmoun, M. Azzaz, J. Nano Res. 52 (2018) 80–87.
[59] R. Bidulský, E. Hryha, J. Bidulská, High Temp. Mater. Process. 35 (2016) 865–870.
[60] E. Hryha, E. Dudrova, in: The Sintering Behaviour of Fe-Mn-C Powder System, Correlation Between Thermodynamics and Sintering Process, Manganese Distribution and Microstructure Composition, Effect of Alloying Mode, InTechOpen, Gothenburg, 2011, pp. 573–602.
[61] Z. Xu, M.A. Hodgson, K. Chang, G. Chen, X. Yuan, P. Cao, Metals 7 (2017) 81.
[62] R. Kononov, O. Ostrovski, S. Ganguly, Metall. Mater. Trans. B 39 (2008) 662–668.
[63] Z. Wang, S. Deng, Q. Zhang, J. Li, Q. Lin, J. Alloys Compd. 890 (2022) 161804.
[64] E. Hryha, E. Dudrova, S. Bengtsson, Powder Metall. 51 (2008) 340–342.
[65] S.-J. Oh, D. Park, K. Kim, I.-J. Shon, S.-J. Lee, Mater. Sci. Eng. A 725 (2018) 382–388.
[66] M. Koyama, T. Sawaguchi, T. Lee, C.S. Lee, K. Tsuzaki, Mater. Sci. Eng. A 528 (2011) 7310–7316.
[67] C. Liang, G. Song, W. Wang, I. Sohn, J. Zeng, J. Mater. Res. Technol. 28 (2024) 2116–2126.
[68] R. Tolouei, J. Harrison, C. Paternoster, S. Turgeon, P. Chevallier, D. Mantovani, Phys. Chem. Chem. Phys. 18 (2016) 19637–19646.
[69] S. Zhu, N. Huang, L. Xu, Y. Zhang, H. Liu, H. Sun, Y. Leng, Mater. Sci. Eng. C 29 (2009) 1589–1592.
[70] M. Salama, M.F. Vaz, R. Colaço, C. Santos, M. Carmezim, J. Funct. Biomater. 13 (2022) 72.
[71] R. Gorejová, L. Haverová, R. Oriňaková, A. Oriňak, M. Oriňak, J. Mater. Sci. 54 (2019) 1913–1947.
[72] H. Hermawan, D. Dubé, D. Mantovani, J. Biomed. Mater. Res. 93 (2010) 1–11.
[73] T. Huang, Y. Zheng, Y. Han, Regen. Biomater. 3 (2016) 205–215.
[74] J. Hufenbach, H. Wendrock, F. Kochta, U. Kühn, A. Gebert, Mater. Lett. 186 (2017) 330–333.
[75] A. Gebert, F. Kochta, A. Voß, S. Oswald, M. Fernandez-Barcia, U. Kühn, J. Hufenbach, Mater. Corros. 69 (2018) 167–177.
[76] J.-S. Lee, K. Fushimi, T. Nakanishi, Y. Hasegawa, Y.-S. Park, Corros. Sci. 89 (2014) 111–117.
[77] L. Chang, M.G. Burke, K. Mukahiwa, J. Duff, Y. Wang, F. Scenini, Corros. Sci. 189 (2021) 109600.
[78] S. Kumar, A. Kumar, R.Madhusudhan Vinaya, R. Sah, S. Manjini, J. Mater. Eng. Perform. 28 (2019) 3600–3613.
[79] M. Heiden, E. Nauman, L. Stanciu, Adv. Healthc. Mater. 6 (2017) 1700120.
[80] J. Čapek, J. Kubásek, D. Vojtěch, E. Jablonská, J. Lipov, T. Ruml, Mater. Sci. Eng. C. 58 (2016) 900–908.
[81] J. Hufenbach, F. Kochta, H. Wendrock, A. Voß, L. Giebeler, S. Oswald, S. Pilz, U. Kühn, A. Lode, M. Gelinsky, Mater. Des. 142 (2018) 22–35.
[82] J. Syarif, Y. Pratesa, Y. Prasetyo, S. Harjanto, Metals 11 (2021) 1597.